Mathematical and Computer Modelling of Dynamical Systems
Vol. 00, No. xx, June 2010, 1–23

RESEARCH ARTICLE

Comparison and combination of reduced order modelling techniques in 3D parametrized heat transfer problems

Fabrizio Gelsomino, Gianluigi Rozza
EPFL, MATHICSE-CMCS
Station 8, CH1015
Lausanne
Switzerland
fabrizio.gelsomino@epfl.ch, gianluigi.rozza@epfl.ch
(*Received 15 April 2010; final version received 30 June 2010*)

Reduced Basis (RB) method has successfully been used in 2D to solve heat transfer parametrized problems. In this work, we present some 3D applications in the same field. We consider two problems, the steady *Thermal Fin* and the time dependent *Graetz Flow*, we compare two reduced order modelling techniques: *RB* and *Proper Orthogonal Decomposition* (*POD*), then we apply a combination of the two strategies in the time dependent case.

1. Introduction

Computing the solution of partial differential equations (PDEs) is very expensive. For realistic simulations, we need thousands degrees of freedom (DoF) in order to obtain good approximations of the solution. For example, for the analysis and the optimization of an engineering system, we have to compute several solutions of the PDEs. We may be interested in outputs depending on the state solution: i.e. maximum or average temperature, heat transfer rates, flow rates, etc. The introduction of some parameters leads to *input-output relationships*. The input-parameter may represent boundary conditions and sources, geometric configurations or physical properties. Classical discretization methods like finite element, finite volume or spectral methods are not the most appropriate. Consequently, we have to develop techniques that reduce the cost and time of the computations. These techniques are called *reduced order methods (ROM)*. The reduced basis (RB) method is one of them and is indicated to evaluate very quickly the outputs mentioned earlier.[1] Moreover, the goal of the reduced basis method is to reduce the complexity of a system without loss of information or the accuracy of the results. This method does not replace any discretization method, like the finite element (FE) method, but there is a collaboration with it. The idea is to start with some selected FE solutions, each of them of dimension $\mathcal{N}$, due to the nodal discretization and then to construct a RB space made up of just N of these basis functions, where $N << \mathcal{N}$. The RB method is particularly well suited in two contexts: the *real-time context*

[1] A brief historical introduction on reduced basis can be found in [11]. Almroth, Stern and Brogan [6] studied the method for one parameter problem. Then with Noor [10] the method was extended to multi-parameter and non-linear problems in structural analysis and only later in fluid dynamics. Current research is dedicated to the development of a posteriori error estimation procedure and to the development of effective sampling strategies for many parameters spaces, in order to improve convergence and computational efficiency [14].

ISSN: 1387-3954 print/ISSN 1744-5051 online

DOI: 10.1080/1387395YYxxxxxxxx
http://www.informaworld.com

and the *many-query context*. The real-time context arises in applications like control engineering and in parameter estimations. The many-query context is involved in multiscale, multiphysics and optimization problems.

In this work, we essentially treat *affine coercive elliptic problems* [14]. The affine parameter-dependence hypothesis enables an efficient *Offline-Online* computation. The reduced basis method reduces notably the Online cost providing much effort and preparation in the Offline step. So, this method is optimized for problems that allow rapid Online computation at the cost of a bigger Offline effort, since the Offline part depends on $\mathcal{N}$, while the Online part depends only on N.

In this work, we will use the RB method to solve 3D conduction and convection problems: *the steady thermal fin problem* and *the time-dependent Graetz flow problem*.

In this paper, we are more interested in extending results about convergence and computational time for RB method applied to 3D problems focusing on heat transfer, both steady and time dependent, problems in order to show that the RB method can also be used for more complex problems. Very recent works dealing with 3D steady applications by reduced basis method are [14] with a linear elasticity block and [18] with an electromagnetic scattering problem.

In the following section, we will review the main ingredients of the RB method for affine coercive elliptic problems and a sampling strategy. We will treat the geometric variations and the constructions of affine mappings, then we recall the *a posteriori error bounds*.

The third section is the continuation of the previous one, where we extend our attention to *parabolic* problems. We will introduce the main changes arising with the time-dependency.

In the fourth section, we present the steady 3D thermal fin problem (see [3], [5] and [8]) which is a steady heat conduction problem with parametrized geometry and physics, previously solved in the 2D case (see [1]). We will give a description of the problem and its mathematical formulation and we present some convergence results for the reduced basis method and a comparison with another ROM technique: POD. The behaviour of the parametrized output is discussed too.

In section five, we solve the time dependent Graetz flow problem (see [4], [5] and [15]), modelling heat conduction and forced heat convection in a duct. As done for the thermal fin, we will introduce the mathematical description of the problem and some numerical results by solving the problem with reduced basis method.

2. Overview of the Reduced Basis Method for Elliptic Problems

We will present the RB methodology for compliant, coercive affine elliptic problem after giving the *exact* formulation (in weak form) of the problem and building upon a finite element discretization. The last part deals with the construction of a posteriori error bounds. For more details see [14] and [11].

2.1. *Elliptic coercive parametric PDEs: compliant case*

2.1.1. Exact Problem formulation

Let $\Omega \in R^d$, $d = 1, 2, 3$ be a suitable physical domain with Lipschitz continuous boundary $\partial\Omega$. Let $\mathcal{D} \subset R^P$ the parameter domain. Let $X^e(\Omega)$ be a Hilbert function space such that $\left(H_0^1(\Omega)\right)^\nu \subset X^e(\Omega) \subset \left(H^1(\Omega)\right)^\nu$ where $\nu = 1$ (respectively $\nu = d$) for a scalar (respectively, vector) field. Here, $H^1(\Omega) =$

$\left\{v \in L^2(\Omega) \,|\, \nabla v \in \left(L^2(\Omega)\right)^d\right\}$, $H_0^1(\Omega) = \left\{v \in H^1(\Omega) \,|\, v_{\partial\Omega} = 0\right\}$, and $L^2(\Omega) = \left\{v \,\text{measurable} \,|\, \int_{\partial\Omega} v^2 \,\text{is finite}\right\}$. We associate to X^e an inner product and a norm, equivalent to the H^1 norm, denoted by $(\cdot,\cdot)_{X^e}$ and $\|\cdot\|_{X^e}$ respectively whose definitions will be given below. Let $a : X^e \times X^e \times \mathcal{D} \longrightarrow R$ be a continuous coercive parametric bilinear form. Let f be a continuous parametric linear functional. We consider the following problem: given $\boldsymbol{\mu} \in R^P$ evaluate $s^e(\boldsymbol{\mu}) = \ell(u^e(\boldsymbol{\mu}); \boldsymbol{\mu})$, where $u^e(\boldsymbol{\mu}) \in X^e(\Omega)$ satisfies:

$$a\left(u^e(\boldsymbol{\mu}), v; \boldsymbol{\mu}\right) = f(v; \boldsymbol{\mu}), \quad \forall v \in X^e. \tag{1}$$

The superscript ^{e} refers to *exact*. Here $\boldsymbol{\mu}$ is the input parameter, s^e is the scalar output, ℓ is the linear output functional and $u(\boldsymbol{\mu})$ is the field variable. Under the hypothesis on the forms a and f the problem (1) has a unique solution. Moreover, we assume that f and ℓ are bounded over X^e and that we have the following affine developments

$$\ell(v; \boldsymbol{\mu}) = \sum_{q=1}^{Q_l} \theta_l^q(\boldsymbol{\mu}) \ell^q(v), \quad f(v; \boldsymbol{\mu}) = \sum_{q=1}^{Q_f} \theta_f^q(\boldsymbol{\mu}) f^q(v) \quad \forall v \in X^e, \forall \boldsymbol{\mu} \in \mathcal{D}, \tag{2}$$

$$a(w, v; \boldsymbol{\mu}) = \sum_{q=1}^{Q_a} \theta_a^q(\boldsymbol{\mu}) a^q(w, v) \quad \forall w, v \in X^e, \forall \boldsymbol{\mu} \in \mathcal{D}, \tag{3}$$

for finite and relatively small Q_l, Q_f, Q_a. We consider that the θ_k^q for $1 \le q \le Q_k$, $k = l$, f, a are simple algebraic expressions that can be readily evaluated in $\mathcal{O}(1)$ operations. Till the end of this section, we will consider *compliant* problems, i.e. we assume that: (i) a is symmetric and (ii) $\ell = f$ for simplicity.[2]

2.1.2. Truth approximation

We introduce the *truth* approximation upon which we will construct the reduced basis (RB) approximation. Moreover, we will measure the error in the reduced basis approximation relative to this truth approximation (see Section 2.4).

We now consider the space $X^{\mathcal{N}} \subset X^e$ such that $\dim(X^{\mathcal{N}}) = \mathcal{N} < \infty$, and we take the Galerkin projection: given $\boldsymbol{\mu} \in R^P$ evaluate $s^e(\boldsymbol{\mu}) = f(u^e(\boldsymbol{\mu}); \boldsymbol{\mu})$ where $u^e(\boldsymbol{\mu}) \in X^e(\Omega)$ satisfies $a\left(u^{\mathcal{N}}(\boldsymbol{\mu}), v; \boldsymbol{\mu}\right) = f(v; \boldsymbol{\mu}), \quad \forall v \in X^{\mathcal{N}}$. Typically, we take $\mathcal{N}$ large to obtain $|s^e(\boldsymbol{\mu}) - s^{\mathcal{N}}(\boldsymbol{\mu})|$ very small. Then, the reduced basis will be built on this truth approximation. For $w, v \in X^e$, we define the *energy inner product* and the *energy norm* respectively as $(w, v)_{\boldsymbol{\mu}} = a(w, v; \boldsymbol{\mu})$, and $\|w\|_{\boldsymbol{\mu}} = \sqrt{(w, w)_{\boldsymbol{\mu}}}$. Moreover, for a given $\overline{\boldsymbol{\mu}} \in \mathcal{D}$, we define the X^e-inner product and the X^e-norm for $w, v \in X^e$ respectively as $(w, v)_X = (w, v)_{\overline{\boldsymbol{\mu}}} + \tau (w, v)_{L^2(\Omega)}$ and $\|w\|_X = \sqrt{(w, w)_X}$, where τ is a non-negative real parameter and $(w, v)_{L^2(\Omega)} = \int_\Omega wv \, d\Omega$. Since $X^{\mathcal{N}} \subset X^e$, the inner products and the norms defined above are the same for the space $X^{\mathcal{N}}$[3]. Now, we can define precisely the exact and discretized coercivity constants, respectively, as $\alpha^e(\boldsymbol{\mu}) = \inf_{w \in X^e} \dfrac{a(w, w; \boldsymbol{\mu})}{\|w\|_X^2}$ and $\alpha^{\mathcal{N}}(\boldsymbol{\mu}) = \inf_{w \in X^{\mathcal{N}}} \dfrac{a(w, w; \boldsymbol{\mu})}{\|w\|_X^2}$. From the coercivity hypothesis, we have that $\alpha^e(\boldsymbol{\mu}) \ge \alpha_0 > 0$, $\forall \boldsymbol{\mu} \in \mathcal{D}$, and from hypothesis

[2] We may extend the methodology to the *non-compliant case* with the introduction of a *dual problem* [14].
[3] The choice of $\overline{\boldsymbol{\mu}}$ and τ will affect the quality and efficiency of our reduced basis a posteriori error estimators, but will not affect directly our reduced basis output predictions (see [14]).

on $X^{\mathcal{N}}$ (conforming space), we have that $\alpha^{\mathcal{N}}(\boldsymbol{\mu}) \geq \alpha^e(\boldsymbol{\mu})$, $\forall \boldsymbol{\mu} \in \mathcal{D}$. In the same way, the continuity constants are defined as $\gamma^e(\boldsymbol{\mu}) = \sup_{w \in X^e} \sup_{v \in X^e} \frac{a(w,v;\boldsymbol{\mu})}{\|w\|_X \|v\|_X}$ and $\gamma^{\mathcal{N}}(\boldsymbol{\mu}) = \sup_{w \in X^{\mathcal{N}}} \sup_{v \in X^{\mathcal{N}}} \frac{a(w,v;\boldsymbol{\mu})}{\|w\|_X \|v\|_X}$, where $\gamma^e(\boldsymbol{\mu})$ is finite for all $\boldsymbol{\mu} \in \mathcal{D}$ and $\gamma^{\mathcal{N}}(\boldsymbol{\mu}) \leq \gamma^e(\boldsymbol{\mu})$, for all $\boldsymbol{\mu} \in \mathcal{D}$.

2.1.3. Reduced basis approximation

The reduced basis approximation is a Galerkin projection on a N-dimensional approximation space that focuses on a low-dimensional, smooth, parametric manifold $\mathcal{M}^{\mathcal{N}} = \{u(\boldsymbol{\mu}) \,|\, \boldsymbol{\mu} \in \mathcal{D}\}$, induced by the parametric dependence. The space $X^{\mathcal{N}}$ is too general because it approximates all members of X^e. So, to approximate a solution $u^{\mathcal{N}}(\boldsymbol{\mu})$ it is sufficient to be able to approximate only functions in $\mathcal{M}^{\mathcal{N}}$. The idea is to choose and compute N basis functions $\xi_1^{\mathcal{N}}, \ldots, \xi_N^{\mathcal{N}} \in \mathcal{M}^{\mathcal{N}}$, called *snapshots* and then, for an arbitrary value $\boldsymbol{\mu}^* \in \mathcal{D}$ compute the solution associated to this parameter (denoted $u_N^{\mathcal{N}}(\boldsymbol{\mu}^*)$) by a linear combinations of $\xi_k^{\mathcal{N}}$, $k = 1, \ldots, N$. More precisely, let N_{max} be an integer, for $N = 1 \ldots N_{max}$, let $X_N^{\mathcal{N}}$ be a N-dimensional subspace of $X^{\mathcal{N}}$. We assume that these spaces satisfy *the nested or hierarchical condition*, i.e.

$$X_1^{\mathcal{N}} \subset \ldots \subset X_{N_{max}}^{\mathcal{N}} \subset X^{\mathcal{N}}. \tag{4}$$

The condition (4) is very important for efficiency and for reducing the computational cost. There are several spaces that satisfy the hierarchical solution, for example Taylor, Lagrange Hermite spaces and POD spaces [11], [14]. In this work, we will focus on *Lagrange spaces* and *POD spaces*. These spaces will be introduced later (see Section 2.2). Now, we consider the Galerkin projection to obtain our reduced basis approximation: given $\boldsymbol{\mu} \in \mathcal{D}$, evaluate $s_N^{\mathcal{N}}(\boldsymbol{\mu}) = f(u_N^{\mathcal{N}}(\boldsymbol{\mu}); \boldsymbol{\mu})$, where $u_N^{\mathcal{N}}(\boldsymbol{\mu}) \in X_N^{\mathcal{N}} \subset X^{\mathcal{N}}$ satisfies

$$a\left(u_N^{\mathcal{N}}(\boldsymbol{\mu}), v; \boldsymbol{\mu}\right) = f(v; \boldsymbol{\mu}), \quad \forall v \in X_N^{\mathcal{N}}. \tag{5}$$

From coercivity and continuity hypothesis on a and f, our conforming reduced basis $X_N^{\mathcal{N}} \subset X^{\mathcal{N}}$, problem (5) admits a unique solution. Moreover, we can demonstrate the well known Galerkin optimality results [11]:

Proposition 2.1: *For any $\boldsymbol{\mu} \in \mathcal{D}$ and $u_N^{\mathcal{N}}(\boldsymbol{\mu})$ and $s_N^{\mathcal{N}}(\boldsymbol{\mu})$ satisfying* (5)

$$\left\|u^{\mathcal{N}}(\boldsymbol{\mu}) - u_N^{\mathcal{N}}(\boldsymbol{\mu})\right\|_{\boldsymbol{\mu}} = \inf_{w_N \in X_N^{\mathcal{N}}} \left\|u^{\mathcal{N}}(\boldsymbol{\mu}) - w_N(\boldsymbol{\mu})\right\|_{\boldsymbol{\mu}}, \tag{6}$$

$$\left\|u^{\mathcal{N}}(\boldsymbol{\mu}) - u_N^{\mathcal{N}}(\boldsymbol{\mu})\right\|_X \leq \sqrt{\frac{\gamma^e(\boldsymbol{\mu})}{\alpha^e(\boldsymbol{\mu})}} \inf_{w_N \in X_N^{\mathcal{N}}} \left\|u^{\mathcal{N}}(\boldsymbol{\mu}) - w_N(\boldsymbol{\mu})\right\|_X, \tag{7}$$

and furthermore for the output (square effect):

$$\begin{aligned} s^{\mathcal{N}}(\boldsymbol{\mu}) - s_N^{\mathcal{N}}(\boldsymbol{\mu}) &= \left\|u^{\mathcal{N}}(\boldsymbol{\mu}) - u_N^{\mathcal{N}}(\boldsymbol{\mu})\right\|_{\boldsymbol{\mu}}^2 \\ &= \inf_{w_N \in X_N^{\mathcal{N}}} \left\|u^{\mathcal{N}}(\boldsymbol{\mu}) - w_N(\boldsymbol{\mu})\right\|_{\boldsymbol{\mu}}^2, \end{aligned} \tag{8}$$

as well as

$$0 < s^{\mathcal{N}}(\boldsymbol{\mu}) - s_N^{\mathcal{N}}(\boldsymbol{\mu}) \leq \gamma^e(\boldsymbol{\mu}) \inf_{w_N \in X_N^{\mathcal{N}}} \left\|u^{\mathcal{N}}(\boldsymbol{\mu}) - w_N(\boldsymbol{\mu})\right\|_X^2. \tag{9}$$

2.2. *Sample/space assembling strategies*

We recall two sampling strategies to obtain the reduced basis spaces. The first one is the *Proper Orthogonal Decomposition*, (*POD*) and the latter is the *Greedy Lagrange* algorithm. In section 4.4.1 of this work, we will compare these two strategies with some examples.

Let $\Xi_{train} = \{\boldsymbol{\mu}^1_{train}, \dots, \boldsymbol{\mu}^{n_{train}}_{train}\}$ be a finite sample set, called *test sample* of parameters in $\mathcal{D}$. These parameters are often chosen by Monte Carlo methods with respect to a uniform or log-uniform density. We assume that the cardinality of $|\Xi_{train}| = n_{train}$ is very large to cover all the set $\mathcal{D}$. Now, we define the following norms: properly for a function $y : \mathcal{D} \longrightarrow R$, $\|y\|_{L^\infty(\Xi_{train})} = \max_{\boldsymbol{\mu}\in\Xi_{train}} |y(\boldsymbol{\mu})|$, and $\|y\|_{L^p(\Xi_{train})} = (|\Xi_{train}|^{-1} \sum_{\boldsymbol{\mu}\in\Xi_{train}} |y|^p(\boldsymbol{\mu}))^{1/p}$.

For a function $z : \mathcal{D} \longrightarrow X^{\mathcal{N}}$ (or X^e) we then define in the same way, $\|z\|_{L^\infty(\Xi_{train};X)} = \max_{\boldsymbol{\mu}\in\Xi_{train}} \|z(\boldsymbol{\mu})\|_X$, and $\|z\|_{L^p(\Xi_{train};X)} = (|\Xi_{train}|^{-1} \sum_{\boldsymbol{\mu}\in\Xi_{train}} \|z(\boldsymbol{\mu})\|^p_X)^{1/p}$.

2.2.1. POD RB spaces

The POD approach ([19]) is popular most notably in time-domain reduced order modelling (see [16]). This technique can also be applied within the parametric context, as we now describe (see [11]).
Given Ξ_{train}, we define the POD RB spaces $X_N^{\mathcal{N}\,POD}$ as the solution of the optimization problem

$$X_N^{\mathcal{N}\,POD} = \arg \inf_{X_N^{\mathcal{N}\,POD} \subset span\{u^{\mathcal{N}}(\boldsymbol{\mu})\,|\,\boldsymbol{\mu}\in\Xi_{train}\}} \left\| u^{\mathcal{N}} - \Pi_{X_N^{\mathcal{N}}} u^{\mathcal{N}} \right\|_{L^2(\Xi_{train};X)}, \qquad (10)$$

where $\Pi_{X_N^{\mathcal{N}}} : X^{\mathcal{N}} \longrightarrow X_N^{\mathcal{N}}$ refers to the orthogonal projection in the X-inner product. Now, we define the correlation matrix $C^{POD} \in R^{n_{train}\times n_{train}}$ given by

$$C^{POD}_{ij} = |\Xi_{ntrain}|^{-1} \left(u^{\mathcal{N}}(\boldsymbol{\mu}^i_{train}), u^{\mathcal{N}}(\boldsymbol{\mu}^j_{train}) \right)_X \quad 1 \le i,j \le n_{train}. \qquad (11)$$

If we express $u^{\mathcal{N}}(\boldsymbol{\mu}^k_{train})$ as $u^{\mathcal{N}}(\boldsymbol{\mu}^k_{train}) = \sum_{q=1}^{\mathcal{N}} u^q(\boldsymbol{\mu}^k_{train})\phi^{FE}_q$, $\forall 1 \le k \le n_{train}$, and if we define the vector $\boldsymbol{u}(\boldsymbol{\mu}^k_{train}) = [u^1(\boldsymbol{\mu}^k_{train}), \dots, u^{\mathcal{N}}(\boldsymbol{\mu}^k_{train})]^T$ and the matrix $Z \in R^{\mathcal{N}\times\mathcal{N}}$ such that $Z_{ij} = \left(\phi^{FE}_j, \phi^{FE}_i\right)_X$, we have that $C^{POD}_{ij} = |\Xi|^{-1}(\boldsymbol{u}(\boldsymbol{\mu}^i_{train}))^T Z(\boldsymbol{u}(\boldsymbol{\mu}^j_{train}))$. We then solve the following eigenproblem: find $(\boldsymbol{\psi}^{POD,\,k}, \lambda^{POD,\,k}) \in R^{n_{train}} \times R^*_+$, $1 \le k \le n_{train}$ such that

$$C^{POD}\boldsymbol{\psi}^{POD,\,k} = \lambda^{POD,\,k}\boldsymbol{\psi}^{POD,\,k}, \text{ and } \left(\boldsymbol{\psi}^{POD,\,i}\right)^T Z\boldsymbol{\psi}^{POD,\,j} = \delta_{ij}. \qquad (12)$$

Arranging the eigenvalues in descending order $\lambda^{POD,\,1} \ge \lambda^{POD,\,2} \ge \dots \ge \lambda^{POD,\,n_{train}} \ge 0$, we define $\Psi^{POD,\,k} \in Z$, $1 \le k \le n_{train}$ as $\Psi^{POD,\,k} = \frac{1}{\sqrt{\lambda^{POD,\,k}}} \sum_{m=1}^{n_{train}} \psi^{POD,\,k}_m u^{\mathcal{N}}(\boldsymbol{\mu}^m_{train})$. We take N_{max} as the smallest N such that $\sqrt{\sum_{k=N+1}^{n_{train}} \lambda^{POD,\,k}} \le \varepsilon_{tol,\,min}$. We then construct the POD RB spaces as $X_N^{\mathcal{N}\,POD} = span\{\Psi^{POD,\,n},\, 1 \le n \le N\}$, $1 \le N \le N_{max}$. We then take $X_N = X_N^{\mathcal{N}\,POD}$ as

our reduced basis space for the choice $\xi^n = \Psi^{POD,\,n}$, $1 \leq n \leq N$.

To use a POD approach we have to compute all solution $u^{\mathcal{N}}(\boldsymbol{\mu})$ for all $\boldsymbol{\mu} \in \Xi_{train}$. The most expensive part is the construction of the correlation matrix and then the resolution of several eigenproblems (12), but POD is very useful for some small n_{train} and that is the reason why it is used in time dependent applications.

2.2.2. Greedy Lagrange spaces

The idea of this strategy is starting with a Ξ_{train}, to select N parameters $\boldsymbol{\mu}^1, \ldots, \boldsymbol{\mu}^N$ and to form the reduced basis space $X_N = span\left\{\xi_n = u^{\mathcal{N}}(\boldsymbol{\mu_n}),\, 1 \leq n \leq N\right\}$ (see [14]). For the greedy approach, we need a sharp, rigorous and efficient bound $\Delta_N^{en}(\boldsymbol{\mu})$ for the reduced basis error $\left\|u^{\mathcal{N}}(\boldsymbol{\mu}) - u_N(\boldsymbol{\mu})\right\|_X$, where u_N is the RB approximation associated with the space X_N. We now present the greedy algorithm. We define $\overline{N}_{max}$ an upper bound for N_{max}, $\varepsilon_{tol,\,min}$ a tolerance of the error. Given Ξ_{train}, $S_1 = \left\{\boldsymbol{\mu}^1\right\}$ and $X_1 = span\left\{u^{\mathcal{N}}(\boldsymbol{\mu}^1)\right\}$,

For $N = 2 : \overline{N}_{max}$

$\boldsymbol{\mu}^N = \arg \max_{\boldsymbol{\mu} \in \Xi_{train}} \Delta_{N-1}^{en}(\boldsymbol{\mu})$;

if $\Delta_{N-1}^{en}(\boldsymbol{\mu}^N) \leq \varepsilon_{tol,\,min}$

$N_{max} = N - 1$;

end;

$S_N = S_{N-1} \cup \boldsymbol{\mu}^N$;

$X_N = X_{N-1} + span\left\{u^{\mathcal{N}}(\boldsymbol{\mu}^N)\right\}$;

end.

With POD we have to compute the snapshots for all $\boldsymbol{\mu} \in \Xi_{train}$, here we only have to compute N_{max} snapshots. In this strategy we use a posteriori error bound $\Delta_N^{en}(\boldsymbol{\mu})$ to approximate the expensive true error $\left\|u^{\mathcal{N}}(\boldsymbol{\mu}) - u_N(\boldsymbol{\mu})\right\|_X$ [4].

2.3. *Geometric variations*

If we want to consider geometric variations of the domain, we have to assume that *the reference domain* Ω is the pre-image of the parameter-dependent *original* domain $\Omega_o(\boldsymbol{\mu})$. For more details, the reader can refer to [14]. We shall assume that, for all $\boldsymbol{\mu}$ in $\mathcal{D}$, we have a domain decomposition of $\Omega_o(\boldsymbol{\mu})$,

$$\overline{\Omega}_o(\boldsymbol{\mu}) = \cup_{k=1}^{K_{dom}} \overline{\Omega}_o^k(\boldsymbol{\mu}) \;, \tag{13}$$

where the $\Omega_o^k(\boldsymbol{\mu}), 1 \leq k \leq K_{dom}$, are mutually non-overlapping open subdomains,

$$\Omega_o^k(\boldsymbol{\mu}) \cap \Omega_o^{k'}(\boldsymbol{\mu}) = \emptyset, \quad 1 \leq k < k' \leq K_{dom} \;. \tag{14}$$

This coarse domain decomposition will be denoted *reduced basis (RB) triangulation*. We now choose a value $\boldsymbol{\mu}_{ref} \in \mathcal{D}$ and define our reference domain as $\Omega \equiv \Omega_o(\boldsymbol{\mu}_{ref})$. It is easy to see that $\overline{\Omega} = \cup_{k=1}^{K_{dom}} \overline{\Omega}^k$, and $\Omega^k \cap \Omega^{k'} = \emptyset, \quad 1 \leq$

[4]Note that in theory, the Greedy minimize the error $|u^{\mathcal{N}} - u_N|$ in the L^∞-norm while the POD minimize the projection error in L^2-norm.

$k < k' \leq K_{dom}$. We will build a very fine finite element (FE) subtriangulation of the RB triangulation of Ω. This FE subtriangulation ensures that the FE approximation accurately treats the perhaps discontinuous coefficients (arising from property and geometry variation) associated with the different subdomains and the subtriangulation also plays an important role in the generation of our affine representation (3). We emphasize that $\boldsymbol{\mu}_{ref}$ only affects the accuracy of the underlying FE approximation upon which the RB discretization and *a posteriori* error estimator are built.

A necessary condition for the affine representation (3) is the so called *Affine Geometry Precondition*. This condition says that for any original domain $\Omega_o(\boldsymbol{\mu})$ that admits a domain decomposition (13) there exists *affine* mappings $\mathcal{T}^{aff,k}(\cdot;\boldsymbol{\mu})$: $\Omega^k \rightarrow \Omega_o^k(\boldsymbol{\mu})$, $1 \leq k \leq K_{dom}$, that are (i) individually *bijective*, and (ii) collectively *continuous*, i.e.

$$\mathcal{T}^{aff,k}(\boldsymbol{x};\boldsymbol{\mu}) = \mathcal{T}^{aff,k'}(\boldsymbol{x};\boldsymbol{\mu}), \quad \begin{array}{l} \forall\, \boldsymbol{x} \in \overline{\Omega}^k \cap \overline{\Omega}^{k'} \ , \\ 1 \leq k < k' \leq K_{dom} \ , \end{array} \tag{15}$$

$\forall \boldsymbol{\mu} \in \mathcal{D}$ and such that

$$\overline{\Omega}_o^k(\boldsymbol{\mu}) = \mathcal{T}^{aff,k}(\overline{\Omega}^k;\boldsymbol{\mu}), \quad 1 \leq k \leq K_{dom}{}^5. \tag{16}$$

We now define our (bijective) affine mappings more explicitly: for $1 \leq k \leq K_{dom}$, any $\boldsymbol{\mu}$ in $\mathcal{D}$, and any $\boldsymbol{x} \in \Omega^k$,

$$\mathcal{T}_i^{aff,k}(\boldsymbol{x};\boldsymbol{\mu}) = C_i^{aff,k}(\boldsymbol{\mu}) + \sum_{j=1}^{d} G_{ij}^{aff,k}(\boldsymbol{\mu})\, x_j, \quad 1 \leq i \leq d \ , \tag{17}$$

for given $C^{aff,k}$: $\mathcal{D} \rightarrow R^d$ and $G^{aff,k}$: $\mathcal{D} \rightarrow R^{d\times d}$. We can then define the associated Jacobians

$$J^{aff,k}(\boldsymbol{\mu}) = |det(G^{aff,k}(\boldsymbol{\mu}))|, \quad 1 \leq k \leq K_{dom} \ , \tag{18}$$

where *det* denotes the determinant. Note that the Jacobian is constant in space over each subdomain. We further define, for any $\boldsymbol{\mu} \in \mathcal{D}$,

$$D^{aff,k}(\boldsymbol{\mu}) = (G^{aff,k}(\boldsymbol{\mu}))^{-1}, \quad 1 \leq k \leq K_{dom} \ ; \tag{19}$$

this matrix shall prove convenient in subsequent derivative transformations.

We may interpret our local mappings in terms of a global transformation. In particular, for any $\boldsymbol{\mu} \in \mathcal{D}$, the local mappings (16) induce a global bijective *piecewise-affine* transformation $\mathcal{T}^{aff}(\,\cdot\,;\boldsymbol{\mu})$: $\Omega \rightarrow \Omega_o(\boldsymbol{\mu})$: for any $\boldsymbol{\mu} \in \mathcal{D}$,

$$\mathcal{T}^{aff}(\boldsymbol{x};\boldsymbol{\mu}) = \mathcal{T}^{aff,k}(\boldsymbol{x};\boldsymbol{\mu}), \ k = \min_{k' \in \{1,\ldots,K_{dom}\} \,|\, x \in \overline{\Omega}^{k'}} k'; \tag{20}$$

note the one-to-one property of this mapping (and, hence the arbitrariness of our min choice in (20)) is ensured by the interface condition (15).

---

[5]Note that we purposely define K_{dom} with respect to the *exact* problem, rather than the FE approximation: K_{dom} can not depend on $\mathcal{N}$ (to be meaningful).

2.3.1. Affine Mappings: Single Subdomain

As we consider a single subdomain in this section, we shall suppress the subdomain superscript for clarity of exposition. We shall focus on the three-dimensional case ($d = 3$). The 2D case is detailed in [14]. The affine transformation (17) can be rewritten as

$$\mathcal{T}_i^{aff}(\boldsymbol{x};\boldsymbol{\mu}) = C_i^{aff}(\boldsymbol{\mu}) + \sum_{j=1}^{3} G_{ij}^{aff}(\boldsymbol{\mu})\, x_j, \quad 1 \le i \le d\ ; \tag{21}$$

we shall refer to $C^{aff}(\boldsymbol{\mu}) \in R^3$ and $G^{aff}(\boldsymbol{\mu}) \in R^{3\times 3}$ as the *mapping coefficients*. In this case we have 12 mapping coefficients that entirely define the affine transformation (21). Under our assumption that the mapping is invertible we know that our Jacobian, $J^{aff}(\boldsymbol{\mu})$ of (18), is strictly positive, and that the derivative transformation matrix, $D^{aff}(\boldsymbol{\mu}) = (G^{aff}(\boldsymbol{\mu}))^{-1}$ of (19), is well defined.

The mapping coefficient can be identified by the relationship between 4 non-coplanar pre-image points, or nodes, $(\overline{\boldsymbol{z}}^1, \overline{\boldsymbol{z}}^2, \overline{\boldsymbol{z}}^3, \overline{\boldsymbol{z}}^4) \equiv ((\overline{z}_1^1, \overline{z}_2^1, \overline{z}_3^1), (\overline{z}_1^2, \overline{z}_2^2, \overline{z}_3^2), (\overline{z}_1^3, \overline{z}_2^3, \overline{z}_3^3), (\overline{z}_1^4, \overline{z}_2^4, \overline{z}_3^4))$, in Ω, and 4 parametrized image nodes, $(\overline{\boldsymbol{z}}_o^1(\boldsymbol{\mu}), \overline{\boldsymbol{z}}_o^2(\boldsymbol{\mu}), \overline{\boldsymbol{z}}_o^3(\boldsymbol{\mu}), \overline{\boldsymbol{z}}_o^4(\boldsymbol{\mu})) \equiv ((\overline{z}_{o1}^1, \overline{z}_{o2}^1, \overline{z}_{o3}^1), (\overline{z}_{o1}^2, \overline{z}_{o2}^2, \overline{z}_{o3}^2), (\overline{z}_{o1}^3, \overline{z}_{o2}^3, \overline{z}_{o3}^3), (\overline{z}_{o1}^4, \overline{z}_{o2}^4, \overline{z}_{o3}^4))(\boldsymbol{\mu})$ in $\Omega_o(\boldsymbol{\mu})$. In particular, for given $\boldsymbol{\mu} \in \mathcal{D}$, application of (21) to the selected nodes yields

$$\overline{z}_{oi}^m(\boldsymbol{\mu}) = C_i^{aff}(\boldsymbol{\mu}) + \sum_{j=1}^{3} G_{ij}^{aff}(\boldsymbol{\mu})\, \overline{z}_j^m, \quad \begin{array}{l} 1 \le i \le 3\ , \\ 1 \le m \le 4\ ; \end{array} \tag{22}$$

(22) constitutes 12 independent equations by which to determine the 12 mapping coefficients. To be more explicit in our construction, we first form the matrix $\mathcal{B}^{aff} \in R^{12\times 12}$ (more generally, $R^{(d^2+d)\times(d^2+d)}$), as:

$$\mathcal{B}^{aff} = \begin{bmatrix}
1&0&0&\overline{z}_1^1&\overline{z}_2^1&\overline{z}_3^1&0&0&0&0&0&0\\
0&1&0&0&0&0&\overline{z}_1^1&\overline{z}_2^1&\overline{z}_3^1&0&0&0\\
0&0&1&0&0&0&0&0&0&\overline{z}_1^1&\overline{z}_2^1&\overline{z}_3^1\\
1&0&0&\overline{z}_1^2&\overline{z}_2^2&\overline{z}_3^2&0&0&0&0&0&0\\
0&1&0&0&0&0&\overline{z}_1^2&\overline{z}_2^2&\overline{z}_3^2&0&0&0\\
0&0&1&0&0&0&0&0&0&\overline{z}_1^2&\overline{z}_2^2&\overline{z}_3^2\\
1&0&0&\overline{z}_1^3&\overline{z}_2^3&\overline{z}_3^3&0&0&0&0&0&0\\
0&1&0&0&0&0&\overline{z}_1^3&\overline{z}_2^3&\overline{z}_3^3&0&0&0\\
0&0&1&0&0&0&0&0&0&\overline{z}_1^3&\overline{z}_2^3&\overline{z}_3^3\\
1&0&0&\overline{z}_1^4&\overline{z}_2^4&\overline{z}_3^4&0&0&0&0&0&0\\
0&1&0&0&0&0&\overline{z}_1^4&\overline{z}_2^4&\overline{z}_3^4&0&0&0\\
0&0&1&0&0&0&0&0&0&\overline{z}_1^4&\overline{z}_2^4&\overline{z}_3^4
\end{bmatrix}.$$

We further introduce the vector $V^{aff}(\boldsymbol{\mu})$ of image nodal locations, as: $V^{aff} = \big[\overline{z}_{o1}^1(\boldsymbol{\mu}), \overline{z}_{o2}^1(\boldsymbol{\mu}), \overline{z}_{o3}^1(\boldsymbol{\mu}), \overline{z}_{o1}^2(\boldsymbol{\mu}), \overline{z}_{o2}^2(\boldsymbol{\mu}), \overline{z}_{o3}^2(\boldsymbol{\mu}), \overline{z}_{o1}^3(\boldsymbol{\mu}), \overline{z}_{o2}^3(\boldsymbol{\mu}), \overline{z}_{o3}^3(\boldsymbol{\mu}), \cdots$
$\cdots, \overline{z}_{o1}^4(\boldsymbol{\mu}), \overline{z}_{o2}^4(\boldsymbol{\mu}), \overline{z}_{o3}^4(\boldsymbol{\mu})\big]^T$. We then obtain our affine mappings

$$\Big[C_1^{aff}(\boldsymbol{\mu}), C_2^{aff}(\boldsymbol{\mu}), C_3^{aff}(\boldsymbol{\mu}), G_{11}^{aff}(\boldsymbol{\mu}), G_{12}^{aff}(\boldsymbol{\mu}), G_{13}^{aff}(\boldsymbol{\mu}), G_{21}^{aff}(\boldsymbol{\mu}), G_{22}^{aff}(\boldsymbol{\mu}), \ldots$$
$$\ldots G_{23}^{aff}(\boldsymbol{\mu}), G_{31}^{aff}(\boldsymbol{\mu}), G_{32}^{aff}(\boldsymbol{\mu}), G_{33}^{aff}(\boldsymbol{\mu})\Big]^T = \big(\mathcal{B}^{aff}\big)^{-1} V^{aff}(\boldsymbol{\mu})^6.$$

[6]Note that $\mathcal{B}^{aff}$ is non-singular under our hypothesis of non-coplanar pre-image nodes and independent of $\boldsymbol{\mu}$; the parametric dependence derives from $V^{aff}(\boldsymbol{\mu})$.

To illustrate how the parametric dependence propagates from the (desired) parametrized domain to the mapping coefficients, we give the example of a tetrahedra. We note that parallelepipeds are the most intuitive subdomains to be able to build transformations by hand, invoking the usual translation, dilation, rotation, and shear primitives. However, we can state a parallelism with the 2D case and consider curvy tetrahedra or curvy tetrahedra instead of triangle and curvy triangle. Here, we shall thus focus only on tetrahedra building blocks. Let be a tetrahedra as in Figure 1(a) with vertices $\overline{\boldsymbol{z}}^1 = (1,0,0)$, $\overline{\boldsymbol{z}}^2 = (0,0,0)$, $\overline{\boldsymbol{z}}^3 = (0,1,0)$ and $\overline{\boldsymbol{z}}^4 = (0,0,1)$ that are pre-images nodes of points $\overline{\boldsymbol{z}}_o^1 = (1,0,0)$, $\overline{\boldsymbol{z}}_o^2 = (0,0,0)$, $\overline{\boldsymbol{z}}_0^3 = (0,1,0)$ and $\overline{\boldsymbol{z}}_o^4 = (0,0,\mu_1)$ (Figure 1(b)). The reference domain and the original domain are respectively denoted by Ω and $\Omega_o(\mu_1)$. The pre-images nodes correspond to the image node for a particular value μ_{ref} of the parameter. Here, $\mu_{ref} = 1$, i.e $(\overline{\boldsymbol{z}}^1, \overline{\boldsymbol{z}}^2, \overline{\boldsymbol{z}}^3, \overline{\boldsymbol{z}}^4) = (\overline{\boldsymbol{z}}_o^1(\mu_{ref}), \overline{\boldsymbol{z}}_o^2(\mu_{ref}), \overline{\boldsymbol{z}}_o^3(\mu_{ref}), \overline{\boldsymbol{z}}_o^4(\mu_{ref}))$

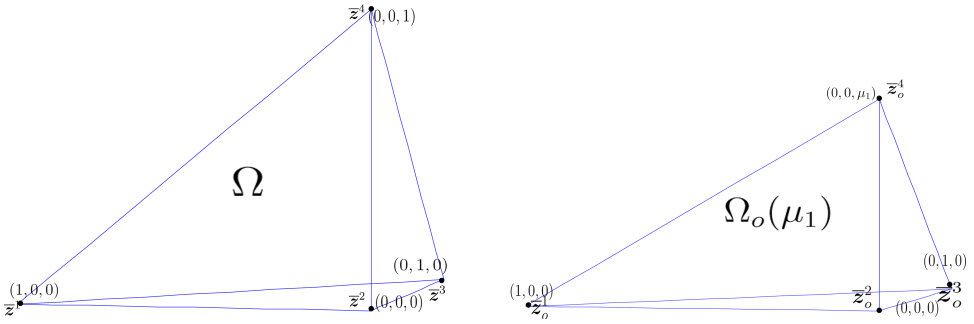

(a) Reference domain Ω. (b) Original domain $\Omega_o(\mu_1)$.

Figure 1. Variation on a tetrahedra

Consequently, we have that $C^{aff}(\mu_1) = 0$ and $G^{aff}(\mu_1) = \begin{bmatrix} 1 & 0 & 0 \\ 0 & 1 & 0 \\ 0 & 0 & \mu_1 \end{bmatrix}$. It follows that $J^{aff}(\mu_1) = \mu_1$ and $D^{aff}(\mu_1) = \begin{bmatrix} 1 & 0 & 0 \\ 0 & 1 & 0 \\ 0 & 0 & \frac{1}{\mu_1} \end{bmatrix}$.

2.4. *A posteriori error bound*

A posteriori error bounds for the reduced basis approximation are crucial for both efficiency and reliability. As regards *efficiency*, error bounds play a role in Offline and Online computational stage. In the Greedy algorithm for example, the application of error bounds permits larger training sample at reduced Offline computational cost. Hence, we have a better accuracy of the reduced basis approximation which can be obtained with a smaller number N of basis functions, and hence we have a reduced Online cost: a posteriori error estimation permits us to control the error which in turn permits us to minimize the computational effort (see [11]). As regards *reliability*, our Offline sampling procedures can not be exhaustive. For a large number of parameters P, there is a large portion of the parameter space $\mathcal{D}$ which remains unexplored. So, the error of a large parts of our parameter domain $\mathcal{D}$ may be uncharacterised. The a posteriori error bounds permit to bound the error for all new parameter value $\boldsymbol{\mu} \in \mathcal{D}$. We can be sure that constraints are satisfied, feasibility conditions are verified, and prognoses are valid (in each case not only for the reduced basis approximation but for the truth finite element solution). So we do not loose any confidence in the solution compared to the underlying FE solution

while exploiting the rapid predictive power of the RB approximation (see [14]).[7]

2.4.1. Error bounds

We define the *residual* $r : \mathcal{D} \longrightarrow \left(X^{\mathcal{N}}\right)'$ as

$$r(v;\boldsymbol{\mu}) = f(v) - a(u_n^{\mathcal{N}}, v, \boldsymbol{\mu}), \tag{23}$$

where $\left(X^{\mathcal{N}}\right)'$ is the *dual* space of $X^{\mathcal{N}}$. We also introduce the function $\hat{e} : \mathcal{D} \longrightarrow X^{\mathcal{N}}$, the Riesz representation of $r(v, \boldsymbol{\mu})$

$$\left(\hat{e}(\boldsymbol{\mu}), v\right)_X = r(v, \boldsymbol{\mu}) \quad \forall v \in X^{\mathcal{N}}. \tag{24}$$

Introducing the *error* $e^{\mathcal{N}}(\boldsymbol{\mu}) = u^{\mathcal{N}} - u_N^{\mathcal{N}} \in X^{\mathcal{N}}$, we have from (24) and (23) that $a(e(\boldsymbol{\mu}), v; \boldsymbol{\mu}) = r(v, \boldsymbol{\mu}) = \left(\hat{e}(\boldsymbol{\mu}), v\right)_X, \quad \forall v \in X$.

We still introduce the *dual norm* $\|r(:, \boldsymbol{\mu})\|_{X'} = \sup_{v \in X} \frac{r(v, \boldsymbol{\mu})}{\|v\|_X} = \|\hat{e}(\boldsymbol{\mu})\|_X$. Note that the second equality follows from the Riesz representation theorem. This definition through the Riesz representation is crucial for the Offline-Online procedure which will be developed below.

We introduce a *lower bound* for $\alpha^{\mathcal{N}}(\boldsymbol{\mu})$, i.e a function $\alpha_{LB}^{\mathcal{N}} : \mathcal{D} \longrightarrow R$ such that $0 < \alpha_{LB}^{\mathcal{N}}(\boldsymbol{\mu}) \leq \alpha^{\mathcal{N}}(\boldsymbol{\mu}), \quad \forall \boldsymbol{\mu} \in \mathcal{D}$ and such that the evaluation $\boldsymbol{\mu} \rightarrow \alpha_{LB}^{\mathcal{N}}(\boldsymbol{\mu})$ is independent of $\mathcal{N}$.[8]

We define now the *energy*, the *output* and *the relative output error bound estimators* [11], respectively, as:

$$\Delta_N^{en}(\boldsymbol{\mu}) = \frac{\|\hat{e}(\boldsymbol{\mu})\|_X}{\left(\alpha_{LB}^{\mathcal{N}}(\boldsymbol{\mu})\right)^{\frac{1}{2}}}, \quad \Delta_N^{s}(\boldsymbol{\mu}) = \frac{\|\hat{e}(\boldsymbol{\mu})\|_X^2}{\alpha_{LB}^{\mathcal{N}}(\boldsymbol{\mu})}, \quad \Delta_N^{s,rel}(\boldsymbol{\mu}) = \frac{\|\hat{e}(\boldsymbol{\mu})\|_X}{\alpha_{LB}^{\mathcal{N}}(\boldsymbol{\mu}) s_N^{\mathcal{N}}(\boldsymbol{\mu})}.$$

We introduce also the *effectivities* as a measure of the quality of the estimators

$$\eta_N^{en}(\boldsymbol{\mu}) = \frac{\Delta_N^{en}}{\|e(\boldsymbol{\mu})\|_{\boldsymbol{\mu}}}, \quad \eta_N^{s}(\boldsymbol{\mu}) = \frac{\Delta_N^{s}(\boldsymbol{\mu})}{s^{\mathcal{N}}(\boldsymbol{\mu}) - s_N^{\mathcal{N}}(\boldsymbol{\mu})}, \quad \eta_N^{s,rel}(\boldsymbol{\mu}) = \frac{\Delta_N^{s,rel}(\boldsymbol{\mu})}{(s^{\mathcal{N}}(\boldsymbol{\mu}) - s_N^{\mathcal{N}}(\boldsymbol{\mu}))/s^{\mathcal{N}}(\boldsymbol{\mu})}.$$

The following proposition shows that these estimators are *rigorous* and *sharp* [14].

Proposition 2.2: *For* $N = 1, 2, \ldots$

$$1 \leq \eta_N^{en}(\boldsymbol{\mu}) \leq \sqrt{\frac{\gamma^e(\boldsymbol{\mu})}{\alpha_{LB}^{\mathcal{N}}(\boldsymbol{\mu})}} \text{ and } 1 \leq \eta_N^{s}(\boldsymbol{\mu}) \leq \frac{\gamma^e(\boldsymbol{\mu})}{\alpha_{LB}^{\mathcal{N}}(\boldsymbol{\mu})}, \quad \forall \boldsymbol{\mu} \in \mathcal{D}.$$

[7]The a posteriori error bound must be *rigorous* (greater or equal to the true error) for all N and all parameters values in the parameter domain $\mathcal{D}$. Non-rigorous error indicators may suffice for adaptivity, but not for reliability. Second, the bound must be reasonably *sharp*. An overly conservative error bound can yield inefficient approximations, typically for N too large. Third, we require *efficiency*, i.e, the cost of the Online evaluation and storage must be $\mathcal{N}$-independent and should be comparable to the cost of the RB output prediction (see [11]).

[8]The $\alpha_{LB}^{\mathcal{N}}$ is computed by the *Successive Constraint Method* (SCM) that is an algorithm to construct lower bounds for the coercivity (and in the non-coercive case, inf-sup stability) constant. This method is based on an Offline-Online computational procedure too and it reduces considerably the Online calculation effort. We will not present the method, but the reader can refer to [14] and [9].

3. Overview of the Reduced Basis Method for Parabolic problems

In this section, we recall *linear parabolic* problems. We focus only on the primal problem,[9] see also [16] and [17]. The *time domain* shall be denoted by $I = [0, t_f]$ where t_f is the *final time*.

3.1. *Reduced Basis and a posteriori error bound*

We introduce the weak form of the $\boldsymbol{\mu}$-parametrized linear parabolic PDE: given $\boldsymbol{\mu} \in \mathcal{D}$, evaluate $s(t;\boldsymbol{\mu}) = \ell(u^e(t;\boldsymbol{\mu});\boldsymbol{\mu})$, where $u^e(t;\boldsymbol{\mu}) \in X^e$ satisfies

$$m\left(\frac{\partial u^e}{\partial t}(t;\boldsymbol{\mu}), v;\boldsymbol{\mu}\right) + a\left(u^e(t;\boldsymbol{\mu}), v;\boldsymbol{\mu}\right) = g(t)f(v;\boldsymbol{\mu}), \quad \forall v \in X^e, \tag{25}$$

with initial condition $u^e(\boldsymbol{x}, t=0;\boldsymbol{\mu}) = u_0^e(\boldsymbol{x};\boldsymbol{\mu})$, where $a(\cdot,\cdot;\boldsymbol{\mu})$ is bilinear, X^e-continuous and coercive, $m(\cdot,\cdot;\boldsymbol{\mu})$ is bilinear, L^2-continuous and coercive and $f(\cdot;\boldsymbol{\mu})$ is linear bounded. The output functional $\ell(\cdot;\boldsymbol{\mu})$ is linear and bounded while $g(\cdot) \in L^2(0,t_f)$ is a *control input*. Moreover, the forms a, m, f and ℓ are affine in $\boldsymbol{\mu}$, as (3) and also m and u_o such that: $\forall \boldsymbol{\mu} \in \mathcal{D}$, $m(v,w;\boldsymbol{\mu}) = \sum_{q=1}^{Q_m} \theta_m^q(\boldsymbol{\mu}) m^q(w,v)$, $\forall w, v \in X^e$ and $u_0(\boldsymbol{x};\boldsymbol{\mu}) = \sum_{q=1}^{Q_u} \theta_u^q(\boldsymbol{\mu}) u_0^q(\boldsymbol{x})$. We now discretize the problem (25) in space (FE) and in time using an *Euler backward* discretization. We introduce Δt as the time step and $n_t = \frac{t_f}{\Delta t}$ as the number of time steps. We still define $t^k = k\Delta t$, $0 \le k \le n_t$, $\mathcal{T} = \{t^0, \dots, t^{n_t}\}$ and $K = \{1, 2, \dots, n_t\}$. Then, we obtain the discretized problem: given $\boldsymbol{\mu} \in \mathcal{D}$, $\forall k \in K$, $\forall v \in X^{\mathcal{N}}$, evaluate $s^{\mathcal{N}\,k}(\boldsymbol{\mu}) = \ell(u^{\mathcal{N}\,k}(\boldsymbol{\mu});\boldsymbol{\mu})$, where $u^{\mathcal{N}\,k}(\boldsymbol{\mu}) \in X^{\mathcal{N}} \subset X^e$, satisfies $m\left(u^{\mathcal{N}\,k}(\boldsymbol{\mu}), v;\boldsymbol{\mu}\right) + \Delta t a\left(u^{\mathcal{N}\,k}(\boldsymbol{\mu}), v;\boldsymbol{\mu}\right) = \Delta t g(t^k) f(v;\boldsymbol{\mu}) + m\left(u^{\mathcal{N}\,k-1}(\boldsymbol{\mu}), v;\boldsymbol{\mu}\right)$, with initial condition $u(\boldsymbol{x}, t_0;\boldsymbol{\mu}) = u_0(\boldsymbol{x};\boldsymbol{\mu})$, where $u_0(\boldsymbol{x},\boldsymbol{\mu})$ is the L^2-projection of $u_0^e(\boldsymbol{x};\boldsymbol{\mu})$. Here, $s^{\mathcal{N}\,k}(\boldsymbol{\mu}) \approx s^e(t^k;\boldsymbol{\mu})$ and $u^{\mathcal{N}\,k} \approx u^e(t^k;\boldsymbol{\mu})$.

The theory we introduced for elliptic problem can be used for the parabolic case. More precisely, we can express our problem in a parameter-independent domain using affine mappings (section 2.3) and we perform a RB approximation (Section 2.1.3). Then, we obtain the reduced problem: $\forall k \in K$, $\forall v \in X^{\mathcal{N}}$ evaluate $s_N^{\mathcal{N}\,k}(\boldsymbol{\mu}) = \ell(u_N^{\mathcal{N}\,k}(\boldsymbol{\mu});\boldsymbol{\mu})$, where $u_N^{\mathcal{N}\,k}(\boldsymbol{\mu}) \in X_N^{\mathcal{N}}$ satisfies $m\left(u_N^{\mathcal{N}\,k}(\boldsymbol{\mu}), v;\boldsymbol{\mu}\right) + \Delta t a\left(u_N^{\mathcal{N}\,k}(\boldsymbol{\mu}), v;\boldsymbol{\mu}\right) = \Delta t g(t^k) f(v;\boldsymbol{\mu}) + m\left(u_N^{\mathcal{N}\,k-1}(\boldsymbol{\mu}), v;\boldsymbol{\mu}\right)$, and, as in the elliptic case, we compute $\alpha_{LB}(\boldsymbol{\mu})$. We define two a posteriori error bounds Δ_N^k and $\Delta_N^{s\,k}$ as in [17]:

$$\Delta_N^k(\boldsymbol{\mu}) = \sqrt{\frac{\frac{\Delta t}{\alpha_{LB}(\boldsymbol{\mu})} \sum_{k'=1}^{k} \left(\epsilon_N^2(t^{k'};\boldsymbol{\mu})(1+\Delta t \alpha_{LB}(\boldsymbol{\mu}))^{k'-1}\right)}{(1+\Delta t \alpha_{LB}(\boldsymbol{\mu}))^k}}, \tag{26}$$

$$\Delta_N^{s\,k}(\boldsymbol{\mu}) = \left(\sup_{v \in X^{\mathcal{N}}} \frac{\ell(v)}{\|v\|_X}\right) \Delta_N^k(\boldsymbol{\mu}), \tag{27}$$

where $\epsilon_N(t^k;\boldsymbol{\mu}) = \left\|r^k(\cdot;\boldsymbol{\mu})\right\|_{(X^{\mathcal{N}})'}$ and $r^k(v;\boldsymbol{\mu})$ is the residual defined as

$$r^k(v;\boldsymbol{\mu}) = \Delta t g(t^k) f(v) + m\left(u_N^{\mathcal{N}\,k-1}(\boldsymbol{\mu}), v;\boldsymbol{\mu}\right) - m\left(u_N^{\mathcal{N}\,k}(\boldsymbol{\mu}), v;\boldsymbol{\mu}\right) - \Delta t a\left(u_N^{\mathcal{N}\,k}(\boldsymbol{\mu}), v;\boldsymbol{\mu}\right),$$

$\forall v \in X^{\mathcal{N}}$, $\forall k \in K$. Then, we have the rigorous and sharp result:

[9] A primal-dual formulation is possible in order to consider non-compliant outputs [20].

Proposition 3.1: *For all $N \in \mathcal{N}$ and for all $k \in K$, $\boldsymbol{\mu} \in \mathcal{D}$:*

$$1 \leq \frac{\Delta_N^k(\boldsymbol{\mu})}{\left\|u^{\mathcal{N}\,k}(\boldsymbol{\mu}) - u_N^{\mathcal{N}\,k}(\boldsymbol{\mu})\right\|_{L^2}} \leq C_1, \quad 1 \leq \frac{\Delta_N^{s\,k}(\boldsymbol{\mu})}{|s^{\mathcal{N}\,k}(\boldsymbol{\mu}) - s_N^{\mathcal{N}\,k}(\boldsymbol{\mu})|} \leq C_2, \tag{28}$$

where C_1 and C_2 are two constants. Moreover,

$$\left\|u^{\mathcal{N}\,k}(\boldsymbol{\mu}) - u_N^{\mathcal{N}\,k}(\boldsymbol{\mu})\right\|_{L^2} \leq \Delta_N^k(\boldsymbol{\mu}), \quad |s^{\mathcal{N}\,k} - s_N^{\mathcal{N}\,k}(\boldsymbol{\mu})| \leq \Delta_N^{s\,k}(\boldsymbol{\mu}). \tag{29}$$

The idea for the construction of the space $X_N^{\mathcal{N}}$, is to consider the set K as a small (time-)parameter sample and the set Ξ_{train} the space-parameter sample (Section 2.2), and to combine POD in time (Section 2.2.1) and the Greedy algorithm (Section 2.2.2) in the parameter space in order to set a *POD-GREEDY sampling procedure* (see [16]). In the next section, we will explain this strategy in details.

3.2. *POD(t)-GREEDY(μ) sampling procedure*

The algorithm, briefly recalled here, is composed of two stages of POD and one stage of Greedy. A previous one stage POD-GREEDY combination has been proposed in [21]. As mentioned before, the POD is used in time while the Greedy is used in the parameter space[10]. We recall that, given L elements $w_j \in X^{\mathcal{N}}$, the POD returns M X-orthogonal functions $\{\Psi_j,\, 1 \leq j \leq M\}$ such that $X_M^{POD} = span\{\Psi_j,\, 1 \leq j \leq M\}$ is optimal in the sense that $X_M^{POD} = arg \inf_{X_M^{POD} \subset span\{w_j,\, 1 \leq j \leq L\}} \left(\frac{1}{L}\sum_{j=1}^{L} \inf_{v \in Y_M} \|w_j - v\|_X^2\right)^{\frac{1}{2}}$.
For simplicity, we will write $X_M^{POD} = POD\left(\{w_j,\, 1 \leq j \leq L\}, M\right)$. The second stage allows us to further reduce the dimension of the approximation space after the first POD in time for a fixed value of the parameter. We introduce the parameter sample Ξ_{train} and an initial parameter $\boldsymbol{\mu}_0 \in \Xi_{train}$ and set $S = \{\boldsymbol{\mu}_0\}$. We give now the algorithm:

Set $Z = \emptyset$;
Set $N = 1$ *and* $\boldsymbol{\mu}_0 = \boldsymbol{\mu}^N$;
While $N \leq N_{max}$
$\{\Psi_j,\, 1 \leq j \leq M_1\} = POD\left(\{u^{\mathcal{N}}(t^k; \boldsymbol{\mu}^N),\, 1 \leq k \leq n_t\}, M_1\right)$;
$Z = Z \cup span\{\Psi_j,\, 1 \leq j \leq M_1\}$;
$N = N + M_2$;
$\{\xi_n,\, 1 \leq n \leq N\} = POD(Z, N)$;
$X_N = span\{\xi_n,\, 1 \leq n \leq N\}$;
$\boldsymbol{\mu}^N = arg \max_{\boldsymbol{\mu} \in \Xi_{train}} \Delta_N^{n_t}(\boldsymbol{\mu})$;
$S = S \cup \boldsymbol{\mu}^N$;
end.

[10] In all this section we will omit the superscript $\mathcal{N}$ for the reduced basis approximations.

Set $X_N = span\{\xi_n,\ 1 \leq n \leq N\}$, $1 \leq N \leq N_{max}$ [11]. Usually we set $1 < M_2 \leq M_1$, see [16] and [17].

4. The 3D steady thermal fin problem

This section is dedicated to the resolution of a steady *thermal fin problem* (see [3], [5]). This problem has already been solved in the 2D case in [1], [8] (see also *http://augustine.mit.edu/workedProblems.htm*). For the 3D case, we used COMSOL [2] linked with the rbMIT software [1] showing that the method can be used with success to solve also more complex problems.

4.1. *Heat Sink: Problem description*

This problem considers the performance of a heat sink designed for the thermal management of high-density electronic components. The main function of a heat sink is to transfer heat from an object at a higher temperature to another at a lower temperature with greater heat capacity. The heat sink comprises of a *base/spreader* which in turn supports a number of *plate fins* exposed to flowing air (see Figure 2(a)). The high density of the heat sink combined with its large area, due to fins, results in the rapid transfer of thermal energy to the surrounding cooler material. Then, the heat sink is cooled and whatever is in direct contact with is also cooled. In our analysis, we shall consider one half of a single fin for symmetry reasons (see Figure 2(b), [8] and [5]). We model the flowing air through a simple convection heat transfer coefficient. Our interest is in the temperature at the base of the spreader.

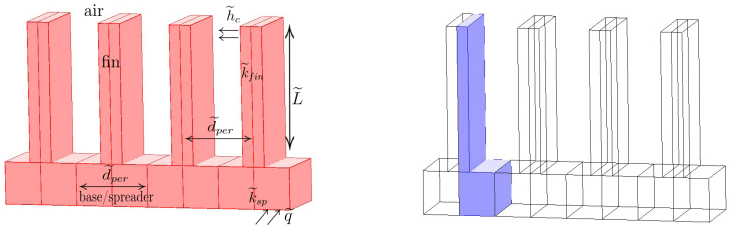

(a) Heat Sink.

(b) Respective Domain for a periodic heat sink.

Figure 2.

From the engineering point of view, this problem illustrates the application of conduction analysis to an important class of cooling problems: electronic components and systems. Examples of systems that require a heat sink to reduce their temperature are microprocessors and refrigeration.

4.1.1. Parametrized geometry and parameters

We introduce the different quantities which describe our problem. The quantities with a tilde $\sim$ correspond to dimensional quantities and the absence of a tilde denotes non-dimensional quantities.
We assume that the spreader has thermal conductivity $\widetilde{k}_{sp}$ and the plate fin has thermal conductivity $\widetilde{k}_{fin}$. The ratio of these conductivities is denoted by $k = \frac{\widetilde{k}_{sp}}{\widetilde{k}_{fin}}$. The distance between two fin is $\widetilde{d}_{per}$ and the height of a fin is denoted by $\widetilde{L}$. We

[11] Note that the complexity remains $\mathcal{O}(\mathcal{N}) + \mathcal{O}(n_{train})$ and is not $\mathcal{O}(\mathcal{N} n_{train})$. The Greedy selects parameter $\boldsymbol{\mu} \in \Xi_{train}$ and then we have to compute all the state solution $u^{\mathcal{N}}(t^k; \boldsymbol{\mu})$ for $1 \leq k \leq n_t$ and apply the POD procedure. Then the second POD procedure gives us spaces of dimension N.

characterize the heat transfer from the fin to the air by a heat transfer coefficient $\widetilde{h}_c$. We consider $P = 3$ parameters, two of them are physical and one is geometrical. The first physical parameter is the Biot number defined as $\mu_1 = Bi = \frac{\widetilde{h}_c \widetilde{d}_{per}}{\widetilde{k}_{fin}}$. The second parameter is $\mu_2 = \frac{\widetilde{L}}{\widetilde{d}_{per}}$, *the non-dimensional fin height* while the third one is given by the conductivity ratio $\mu_3 = k$. The parameter domain is given by $\mathcal{D} = [0.01, 0.5] \times [2, 8] \times [1, 10]$. We denote by $\boldsymbol{\mu}$ the vector of parameters, i.e. $\boldsymbol{\mu} = (\mu_1, \mu_2, \mu_3)$.

The temperature $\widetilde{T}$ is measured relative to the temperature of the air *at infinity*, $\widetilde{T}_{air}$, and non-dimensionalized with respect to $\frac{\widetilde{q}\widetilde{d}_{per}}{\widetilde{k}_{fin}}$ where $\widetilde{q}$ is the dimensional heat flux into the spreader. We identify in Figure 3 the points defining the geometry and the different subdomains $\Omega_o^k(\boldsymbol{\mu})$, $1 \leq k \leq 2$, considered. We define the global domain $\Omega_o(\boldsymbol{\mu})$ as $\Omega_o(\boldsymbol{\mu}) = \Omega_o^1(\boldsymbol{\mu}) \cup \Omega_o^2(\boldsymbol{\mu})$. Since we have only one geometrical parameter, μ_2 and since Ω_o^1 is parameter-independent, we can write $\Omega_o(\boldsymbol{\mu}) = \Omega_o(\mu_2) = \Omega_o^1 \cup \Omega_o^2(\mu_2)$.

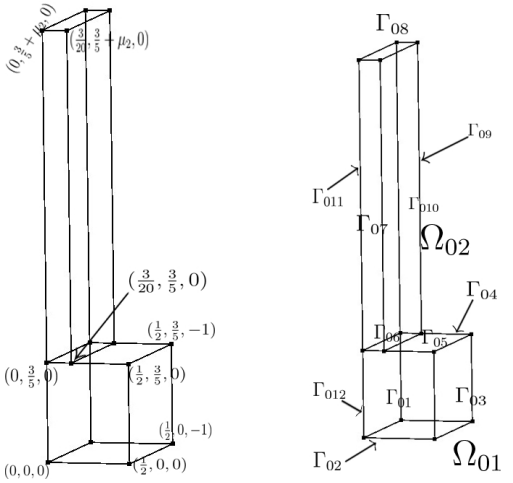

(a) Parametrized Geometry.

(b) Domain Boundaries.

Figure 3.

4.2. *Mathematical formulation*

The non-dimensional temperature $u_o(\boldsymbol{\mu})$ satisfies the conduction equation in $\Omega_o(\mu_2)$. We impose continuity of temperature and heat flux at the spreader-fin interface. Moreover, we impose zero heat flux on the horizontal exposed surfaces of the spreader and fin; uniform heat flux on the spreader base and heat-transfer convection (Robin) boundary conditions on the vertical face of the fin, the one exposed to the flowing air. Mathematically, $u_o(\boldsymbol{\mu})$ satisfies

$$\begin{cases} -\mu_3 \boldsymbol{\Delta} u_o(\boldsymbol{\mu}) = 0 & \text{in } \Omega_o^1, \\ -\Delta u_o(\boldsymbol{\mu}) = 0 & \text{in } \Omega_o^2(\mu_2), \\ \mu_3 \frac{\partial u_o}{\partial \boldsymbol{n}}(\boldsymbol{\mu}) = 1 & \text{on } \Gamma_{o2}, \\ \frac{\partial u_o}{\partial \boldsymbol{n}}(\boldsymbol{\mu}) = 0 & \text{on } \Gamma_{o1,3,4,5,7,8,9,11,12}, \\ \frac{\partial u_o}{\partial \boldsymbol{n}}(\boldsymbol{\mu}) + \mu_1 u_o(\boldsymbol{\mu}) = 0 & \text{on } \Gamma_{o10}\,, \end{cases}$$

where $\boldsymbol{n}$ denotes the unit outward normal. On Γ_{o6}, we impose continuity of temperature and heat flux. The output of interest is $s(\boldsymbol{\mu}) = 2\int_{\Gamma_{o2}} u_o(\boldsymbol{\mu})$, which represents the average of the temperature on the base of the spreader[12]. In this scalar problem we take $X^e = H^1(\Omega_o(\boldsymbol{\mu}))$. The weak formulation reads as follow: *for all* $v \in X^e$, *find* $u_o(\boldsymbol{\mu}) \in X^e$ *such that*

$$\mu_3 \int_{\Omega_o^1} \nabla u_o(\boldsymbol{\mu}) \nabla v + \int_{\Omega_o^2(\mu_2)} \nabla u_o(\boldsymbol{\mu}) \nabla v + \mu_1 \int_{\Gamma_{o10}} u_o(\boldsymbol{\mu}) v = \int_{\Gamma_{o1}} v. \qquad (30)$$

Introducing the bilinear form $a_o(u, v, \boldsymbol{\mu}) = \mu_3 \int_{\Omega_o^1} \nabla u(\boldsymbol{\mu}) \nabla v + \int_{\Omega_o^2(\mu_2)} \nabla u(\boldsymbol{\mu}) \nabla v + \mu_1 \int_{\Gamma_{o10}} u(\boldsymbol{\mu}) v$ and the linear functional $F_o(v, \boldsymbol{\mu}) = \int_{\Gamma_{o1}} v$, we can rewrite (30) as : *find* $u_o(\boldsymbol{\mu}) \in X^e$ *such that* $a_o(u_o(\boldsymbol{\mu}), v, \boldsymbol{\mu}) = F_o(v)$, for all $v \in H^1(\Omega_o(\boldsymbol{\mu}))$.

The coercivity and the continuity of the bilinear form a_o and the continuity of the functional F_o can be proved. So the Lax-Milgram theorem ensures the existence and unicity of the solution (see [12]).

4.3. *Reference geometry*

In order to obtain the affine decomposition of the bilinear form a_o and to work with parameter-independent geometry. We take $\overline{\boldsymbol{\mu}} = (0.3, 2, 5)$ as reference parameter vector (see Section 2.1.2). Then, the reference domain will be $\Omega = \Omega_o(\mu_2 = 2)$. Note that we have $\Omega = \Omega_o^1 \cup \Omega_o^2\,(\mu_2 = 2) = \Omega^1 \cup \Omega^2$, where $\Omega^1 = \Omega_o^1$ and $\Omega^2 = \Omega_o^2\,(\mu_2 = 2)$. We want to construct an affine mapping $\mathcal{T}^{aff,k}(:;\boldsymbol{\mu}) : \Omega^k \longrightarrow \Omega_o^k(\boldsymbol{\mu})$, with $k = 1, 2$. We remind that these mappings have to be *individually bijective*, *collectively continuous* and each mapping has the general form $\mathcal{T}_i^{aff,k}(\boldsymbol{x}, \boldsymbol{\mu}) = C_i^{aff,k} + \sum_{j=1}^d G_{ij}^{aff,k}(\boldsymbol{\mu}) x_j$, $1 \le i \le d$ for given $C^{aff,k} : \mathcal{D} \longrightarrow R^3$ and $G^{aff,k} : \mathcal{D} \longrightarrow R^{3\times 3}$, $k = 1, 2$ (see (17)).
Since Ω_o^1 does not depend of any parameters, we have that $\mathcal{T}^{aff,1} = Id_1$, where $Id_k \colon \Omega^k \times \mathcal{D} \longrightarrow \Omega_o^k(\boldsymbol{\mu})$ is the identity operator, $k = 1, 2$. To construct $\mathcal{T}^{aff,2}$, we choose four non-colinear points in Ω^2 and four parametrized image node in $\Omega_o^2(\boldsymbol{\mu})$. Then, we apply the method developed in Section 2.3 and we obtain $\mathcal{T}^{aff,2}(\boldsymbol{x}, \boldsymbol{\mu}) = \begin{pmatrix} 0 \\ \frac{3}{5} - \frac{3}{10}\mu_2 \\ 0 \end{pmatrix} + \begin{pmatrix} 1 & 0 & 0 \\ 0 & \frac{\mu_2}{2} & 0 \\ 0 & 0 & 1 \end{pmatrix} \boldsymbol{x}$.

4.3.1. Affine decomposition

In order to find the affine decomposition, we start to compute the Jacobian and the matrix $D^{aff,k}$, $k = 1, 2$. For $k = 1$, all these quantities are trivial, i.e. $J^{aff,1} = 1$ and $D^{aff,1} = I$, where $I \in R^{3\times 3}$ is the identity matrix. For $k = 2$, we easily compute $J^{aff,2}(\mu_2) = \frac{\mu_2}{2}$, and $D^{aff,2} = \begin{pmatrix} 1 & 0 & 0 \\ 0 & \frac{2}{\mu_2} & 0 \\ 0 & 0 & 1 \end{pmatrix}$. We obtain the bilinear form expressed in the reference domain : $a(u, v, \boldsymbol{\mu}) = \mu_3 \left(\int_{\Omega^1} \frac{\partial u}{\partial x_1} \frac{\partial v}{\partial x_1} + \int_{\Omega^1} \frac{\partial u}{\partial x_2} \frac{\partial v}{\partial x_2} + \int_{\Omega^1} \frac{\partial u}{\partial x_3} \frac{\partial v}{\partial x_3} \right) + \int_{\Omega^2} \frac{\partial u}{\partial x_1} \frac{\partial v}{\partial x_1} + \frac{2}{\mu_2} \int_{\Omega^2} \frac{\partial u}{\partial x_2} \frac{\partial v}{\partial x_2} + \int_{\Omega^2} \frac{\partial u}{\partial x_3} \frac{\partial v}{\partial x_3} + \frac{\mu_1 \mu_2}{2} \int_{\Gamma_{10}} uv$.

[12]By taking into account the symmetry of the fin configuration, we just consider a half of the fin.

4.4. *Results and Visualizations*

In this section, we give the convergence result of the Greedy algorithm (Section 2.2.2). Here, the sample size is $n_{train} = 3000$, the tolerance $\epsilon_{tol,\,min} = 0.01$ and the $\overline{N}_{max} = 120$. In the Figure 4(a), we have represented for each N the parameter $\boldsymbol{\mu} = (\mu_1, \mu_2, \mu_3)$ chosen automatically by the algorithm. We have obtained $N_{max} = 12$ for the primal problem. In the Figure 4(b), we represent the error bound $\Delta_N(\boldsymbol{\mu})$ for $1 \leq N \leq N_{max}$. We report in Figure 5 the visualization of some representative

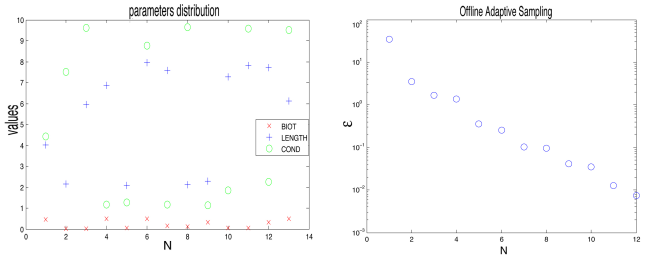

(a) Chosen parameters. (b) Error bound Δ_N.

Figure 4. Sample and error bound for the Greedy.

reduced basis solutions.

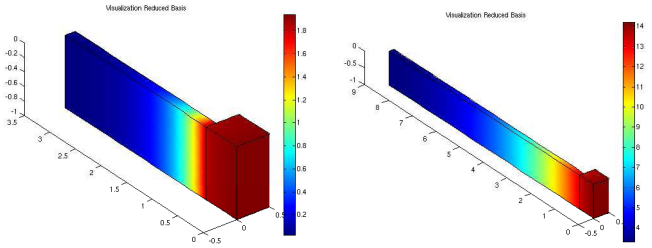

(a) Example of representative solution for $\boldsymbol{\mu} = (0.5, 2.75, 10)$. (b) Example of representative solution for $\boldsymbol{\mu} = (0.01, 8, 1)$

Figure 5.

4.4.1. Comparison between the POD and the Greedy

We compare the Greedy performance with the POD. We recall that theoretically the Greedy-RB has to minimize the RB error in L^∞-norm while the POD minimizes the projection error in L^2-norm. In Figure 6(a) we represent the error in L^2-norm for Greedy-RB and POD approximations while in Figure 6(b), we represent the error in L^∞-norm. We see that the Figure 6(a) confirms the theoretical expectation,

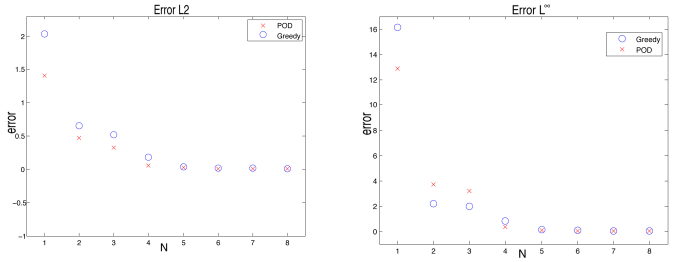

(a) $\|u^{\mathcal{N}} - u_N^{\mathcal{N}}\|_{L^2}$. (b) $\|u^{\mathcal{N}} - u_N^{\mathcal{N}}\|_{L^\infty}$.

Figure 6. Greedy and POD performance comparison.

i.e. the error of the Greedy-RB approximation is bigger that the error of the POD

approximation since we are considering POD in its natural environment, i.e. by considering L^2-norm (and not L^∞). The opposite is valid for POD and Greedy for smaller N in Figure 6(b) in the natural environment for the Greedy. Please, note that the differences are not so significant and we may consider the two approaches as equivalent (in terms of performances).

4.4.2. Output

Just as non-exhaustive example, we present here the variation of the output s_N, i.e, the average of the temperature on the base of the spreader, as a function of the different parameters in 3D (see Figure 7). The error bound over the reported outputs is $\Delta_N^s(\mu) \leq 10^{-4}$ for all μ tested in the range of variation of the parameters. Graphically, the result of Figure 7(a) corresponds to results expected by the theory:

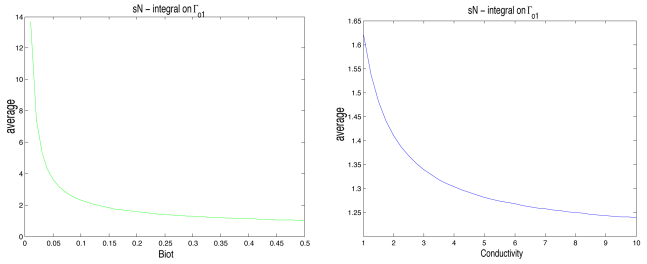

(a) Output with $\mu_2 = 2$ and $\mu_3 = 4$.

(b) Output with $\mu_1 = 0.3$ and $\mu_2 = 2$.

Figure 7.

if the Biot number (μ_1) increases, then there is a bigger heat transfer and so the temperature at the base decreases. In Figure 7(b), we show how the temperature decreases when μ_3 increases.

4.4.3. Computational time

We give some computational times to show the efficiency of the method. We define two kind of computational time :

$$t^{Offline}(\mathcal{N}) = \frac{\text{Offline time to perform SCM \& Greedy}}{\text{time to evaluate } \boldsymbol{\mu} \rightarrow s^{\mathcal{N}}(\boldsymbol{\mu})},$$

that computes the *break-even*, i.e. the maximal number of solutions that we may evaluate with the FE method without using the RB at the same computational cost. We introduce also

$$t^{Online}(\mathcal{N}, N) = \frac{\text{Online time to evaluate } \partial t(\boldsymbol{\mu} \rightarrow s_N)}{\text{time to evaluate } \boldsymbol{\mu} \rightarrow s^{\mathcal{N}}(\boldsymbol{\mu})},$$

where, ∂t is the time we need to evaluate $\boldsymbol{\mu} \rightarrow s_N(\boldsymbol{\mu})$. This computational time shows the gain of time using the RB method for the solution of parametrized problems. We have :

$$t^{Offline}(\mathcal{N}, N) = \frac{674.2}{0.61} \approx 1105, \; t^{Online}(\mathcal{N}, N) = \frac{0.004}{0.61} = 0.006.$$

The break-even $= 1105$ for $\mathcal{N} = 11340$. The computational costs for the RB output calculation is 150 times less expensive than the ones for the FE.

5. The 3D time-dependent Graetz problem

In this section, we will consider a 3D time-dependent non-compliant problem: the *Graetz flow problem* (see [4], [5] and [15]). The 2D case has also be treated in [1] (see also http://augustine.mit.edu/workedProblems.htm).

5.1. *Problem description*

This is a classical problem in literature dealing with forced heat convection combined with heat conduction in a channel, separated in two parts. The first part is made up of cold walls, whereas the second one has hot walls. The temperature at inlet is imposed and the flow has a known given convective field. In Figure 8(a), we can see the duct with the cold and hot portion. The physical domain $\Omega_o(\boldsymbol{\mu}) = \Omega_o^1(\boldsymbol{\mu}) \cup \Omega_o^2(\boldsymbol{\mu})$ is defined in Figure 8(b). We recall that the quantities with a tilde are dimensional quantity. A point $\boldsymbol{x} = (x_{o1}, x_{o2}, x_{o3})$ is non-dimensionalized with respect to $\tilde{h}$ the width of the channel (in the x_{o3}-direction). We introduce also $\tilde{k}$ as the dimensional conductivity coefficient for the air flowing in the channel, $\tilde{\nu}$ the dimensional diffusivity and $\tilde{U}$ the reference velocity for the convective field. The *Péclèt* number is defined as $Pe = \frac{\tilde{U}\tilde{h}}{\tilde{\nu}}$. We consider 3 parameters $\boldsymbol{\mu} = (\mu_1, \mu_2, \mu_3)$. We denote by μ_1 and μ_2 the geometric parameters that represent the height of the cold portion and the length of the hot portion, respectively (see Figure 8(c)). The last one is the Péclèt number that is a physical parameter, i.e. $\mu_3 = Pe$. The parameter domain is given by $\mathcal{D} = [1, 2] \times [2, 10] \times [0.1, 10]$.

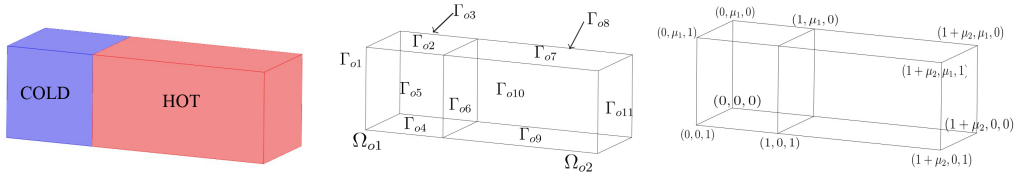

(a) A channel with cold and hot portion.

(b) Domain boundaries.

(c) Parametrized geometry.

Figure 8.

5.2. *Mathematical formulation*

The non-dimensionalized temperature $u_o(\boldsymbol{x}, t; \boldsymbol{\mu})$[13] satisfies the unsteady advection-diffusion equation in $\Omega_o(\boldsymbol{\mu})$. The time interval is $[0, T]$, with T the final time. We impose continuity of temperature and heat flux on all internal faces. At the inflow and on the cold walls, we impose homogeneous Dirichlet boundary condition. On the hot walls, we have non-homogeneous Dirichlet boundary condition and at the outflow we impose zero heat flux (homogeneous Neumann boundary condition)[14].

[13] For convenience, we will not indicate the $\boldsymbol{x}$-dependence of u_o, i.e. we will write $u_o(\boldsymbol{x}, t; \boldsymbol{\mu})$ as $u_o(t; \boldsymbol{\mu})$.

[14] The homogeneous Dirichlet boundaries will be denoted by Γ_{Dh} i.e. $\Gamma_{Dh} = \Gamma_{o1,2,3,4,5}$ and the non-homogeneous Dirichlet boundary will be denoted by Γ_{Dnh}, i.e. $\Gamma_{Dnh} = \Gamma_{o7,8,9,10}$ We denote $\Gamma_D = \Gamma_{Dh} \cup \Gamma_{Dnh}$. The Neumann boundary will be denoted by $\Gamma_N = \Gamma_{o11}$.

Mathematically, $u_o(\boldsymbol{\mu})$ satisfies

$$\begin{cases} \frac{\partial u_o(t;\boldsymbol{\mu})}{\partial t} - \Delta u_o(t;\boldsymbol{\mu}) + x_{o2}(1-x_{o2})\frac{\partial u_o}{\partial x_1}(t;\boldsymbol{\mu}) = 0 & \text{in } \Omega_o(\boldsymbol{\mu}),\ t \in [0,T] \\ u_o(t;\boldsymbol{\mu}) = 0 & \text{on } \Gamma_{o1,2,3,4,5},\ t \in (0,T] \\ u_o(t;\boldsymbol{\mu}) = g(t) & \text{on } \Gamma_{o7,8,9,10},\ t \in (0,T] \\ \frac{\partial u_o}{\partial \boldsymbol{n}}(t;\boldsymbol{\mu}) = 0 & \text{on } \Gamma_{o11},\ t \in (0,T] \\ u_o(t=0;\boldsymbol{\mu}) = 0 & \text{in } \Omega_o(\boldsymbol{\mu}) \end{cases}$$

where $\boldsymbol{n}$ denotes the unit outward normal and $g(t)$ is the *control input*. On Γ_{o6}, we impose continuity of temperature and heat flux. The convective field is $U = x_{o2}(1-x_{o2})$. The output of interest is $s(t;\boldsymbol{\mu}) = \int_0^T \left(\int_{\Omega_o(\boldsymbol{\mu})} u_o(t;\boldsymbol{\mu})\, d\boldsymbol{x} \right) h(t)\, dt$, where $h(t)$ is a function of time. This output represents the average temperature. Let us introduce the space $V = \left\{ v \in H^1(\Omega_o(\boldsymbol{\mu})) \,|\, v = 0 \text{ on } \Gamma_D \right\}$. We will also introduce a lifting of $g(t)$, $R_g \in H^1(\Omega_o(\boldsymbol{\mu})) \times [0,T]$ such that $R_{g|\Gamma_{Dnh}} = g(t)$ and $u_o(t;\boldsymbol{\mu}) = \overline{u}_o(t;\boldsymbol{\mu}) + R_g(\boldsymbol{x},t)$ where $\overline{u}_o \in [0,T] \times V$. We can now give the weak formulation: *for all $v \in V$, find $\overline{u}_o(t;\boldsymbol{\mu}) \in [0,T] \times V$ such that*

$$m_o(\frac{\partial \overline{u}_o}{\partial t}, v; \boldsymbol{\mu}) + a_o(\overline{u}_o, v; \boldsymbol{\mu}) = g(t) F_o(v; \boldsymbol{\mu}) \tag{31}$$

where $a_o(\overline{u}_o, v; \boldsymbol{\mu}) = \frac{1}{\mu_3} \int_{\Omega_o(\boldsymbol{\mu})} \nabla \overline{u}_o(t;\boldsymbol{\mu}) \nabla v + \int_{\Omega_o(\boldsymbol{\mu})} x_{o2}(1-x_{o2}) \frac{\partial \overline{u}_o(t;\boldsymbol{\mu})}{\partial x_{o1}} v$,
$m_o(\frac{\partial \overline{u}_o}{\partial t}, v; \boldsymbol{\mu}) = \int_{\Omega_o(\boldsymbol{\mu})} \frac{\partial \overline{u}_o(t;\boldsymbol{\mu})}{\partial t} v$, and
$F_o(v, \boldsymbol{\mu}) = -\int_{\Omega_o(\boldsymbol{\mu})} \frac{\partial R_g}{\partial t} v - \frac{1}{\mu_3} \int_{\Omega_o(\boldsymbol{\mu})} \nabla R_g \nabla v - \int_{\Omega_o(\boldsymbol{\mu})} x_{o2}(1-x_{o2}) \frac{\partial R_g}{\partial x_{o1}} v$.

The function $g \in L^2(0,T)$. The coercivity and the continuity of the bilinear form a_o and the continuity of the functional F_o can be proved. So the Lax-Milgram theorem ensures the existence and unicity of the solution (see [12]).

5.3. *Reference geometry*

As we did for the thermal fin, we will construct the affine mappings to obtain the affine decomposition of the bilinear form a_o and F_o. In this case, the reference domain $\Omega = \Omega_o(\overline{\boldsymbol{\mu}})$ is given for $\overline{\boldsymbol{\mu}} = (1,2,1)$; while the reference subdomains are $\Omega^k = \Omega_o^k(\overline{\boldsymbol{\mu}})$, $k = 1,2$. We want to construct an affine mapping $\mathcal{T}^{aff,k}(:;\boldsymbol{\mu}) : \Omega^k \longrightarrow \Omega_o^k(\boldsymbol{\mu})$, with $k = 1,2$. In this problem the two subdomains depend on the parameters. We apply the methodology explained in Section 2.3 for the two subdomains and we obtain $\mathcal{T}^{aff,1}(\boldsymbol{x},\boldsymbol{\mu}) = \begin{pmatrix} 1 & 0 & 0 \\ 0 & \mu_1 & 0 \\ 0 & 0 & 1 \end{pmatrix} \boldsymbol{x}$ and $\mathcal{T}^{aff,2}(\boldsymbol{x},\boldsymbol{\mu}) = \begin{pmatrix} 1-\frac{\mu_2}{2} \\ 0 \\ 0 \end{pmatrix} + \begin{pmatrix} \frac{\mu_2}{2} & 0 & 0 \\ 0 & \mu_1 & 0 \\ 0 & 0 & 1 \end{pmatrix} \boldsymbol{x}$. In order to find the affine decomposition, we compute the Jacobian and the matrix $D^{aff,k}$, $k = 1,2$. We obtain that $J^{aff,1}(\boldsymbol{\mu}) = \mu_1$, $J^{aff,2}(\boldsymbol{\mu}) = \frac{1}{2}\mu_1\mu_2$, and $D^{aff,1} = \begin{pmatrix} 1 & 0 & 0 \\ 0 & \frac{1}{\mu_1} & 0 \\ 0 & 0 & 1 \end{pmatrix}$, $D^{aff,2} = \begin{pmatrix} \frac{1}{\mu_2} & 0 & 0 \\ 0 & \frac{1}{\mu_1} & 0 \\ 0 & 0 & 1 \end{pmatrix}$.

We obtain the time-independent bilinear form expressed in the reference domain:

$$a(\overline{u},v,\boldsymbol{\mu}) = \frac{\mu_1}{\mu_3}\int_{\Omega^1}\frac{\partial\overline{u}}{\partial x_1}\frac{\partial v}{\partial x_1} + \frac{1}{\mu_1\mu_3}\int_{\Omega^1}\frac{\partial\overline{u}}{\partial x_2}\frac{\partial v}{\partial x_2} + \frac{\mu_1}{\mu_3}\int_{\Omega^1}\frac{\partial\overline{u}}{\partial x_3}\frac{\partial v}{\partial x_3}$$

$$+\frac{2\mu_1}{\mu_2\mu_3}\int_{\Omega^2}\frac{\partial\overline{u}}{\partial x_1}\frac{\partial v}{\partial x_1} + \frac{\mu_2}{2\mu_1\mu_3}\frac{2}{\mu_2}\int_{\Omega^2}\frac{\partial\overline{u}}{\partial x_2}\frac{\partial v}{\partial x_2}$$

$$+\frac{\mu_1\mu_2}{2\mu_3}\int_{\Omega^2}\frac{\partial\overline{u}}{\partial x_3}\frac{\partial v}{\partial x_3} + \mu_1\int_{\Omega^1}x_2(1-x_2)\frac{\partial\overline{u}}{\partial x_1}v + \mu_1\int_{\Omega^2}x_2(1-x_2)\frac{\partial\overline{u}}{\partial x_1}v.$$

In the same way we obtain the time-dependent bilinear form $m(\frac{\partial\overline{u}}{\partial t},v;\boldsymbol{\mu}) = \mu_1\int_{\Omega^1}\frac{\partial\overline{u}}{\partial t}v + \mu_1\int_{\Omega^2}\frac{\partial\overline{u}}{\partial t}v$, and the linear functional

$$F(v;\boldsymbol{\mu}) = -\frac{\mu_1}{\mu_3}\int_{\Omega^1}\frac{\partial R_g}{\partial x_1}\frac{\partial v}{\partial x_1} - \frac{1}{\mu_1\mu_3}\int_{\Omega^1}\frac{\partial R_g}{\partial x_2}\frac{\partial v}{\partial x_2} - \frac{\mu_1}{\mu_3}\int_{\Omega^1}\frac{\partial R_g}{\partial x_3}\frac{\partial v}{\partial x_3} - \frac{2\mu_1}{\mu_2\mu_3}\int_{\Omega^2}\frac{\partial R_g}{\partial x_1}\frac{\partial v}{\partial x_1}$$

$$-\frac{\mu_2}{2\mu_1\mu_3}\frac{2}{\mu_2}\int_{\Omega^2}\frac{\partial R_g}{\partial x_2}\frac{\partial v}{\partial x_2} - \frac{\mu_1\mu_2}{2\mu_3}\int_{\Omega^2}\frac{\partial R_g}{\partial x_3}\frac{\partial v}{\partial x_3} - \mu_1\int_{\Omega^1}x_2(1-x_2)\frac{\partial R_g}{\partial x_1}v$$

$$-\mu_1\int_{\Omega^2}x_2(1-x_2)\frac{\partial R_g}{\partial x_1}v - \mu_1\int_{\Omega^1}\frac{\partial R_g}{\partial t}v - \mu_1\int_{\Omega^2}\frac{\partial R_g}{\partial t}v.$$

The affine decomposition is $a(\overline{u},v;\boldsymbol{\mu}) = \sum_{q=1}^{8}\theta_a^q(\boldsymbol{\mu})a^q(\overline{u},v)$, $m(\frac{\partial\overline{u}}{\partial t},v;\boldsymbol{\mu}) = \sum_{q=1}^{2}\theta_m^q(\boldsymbol{\mu})m^q(\frac{\partial\overline{u}}{\partial t},v;\boldsymbol{\mu})$, and $F(v;\boldsymbol{\mu}) = \sum_{q=1}^{10}\theta_f^q f^q(v;\boldsymbol{\mu})$. The quantities $\theta_a^q, a^q, \theta_m^q, m^q, \theta_f^q, f^q$ can easily be deduced from the definition of the forms a, m and F.

5.4. *Results and Visualization*

We show the results of the POD-Greedy-RB algorithm described in Section 3.2. Here, the sample size is $n_{train} = 3000$, the tolerance $\epsilon_{tol,min} = 0.01$ and the $\overline{N}_{max} = 120$ (Section 3.2). Since the problem is non-compliant, we have to do the POD-Greedy for the primal and dual problem (see [20]). In the Figure 9(a) and 10(a), we have represented for each N the parameter $\boldsymbol{\mu} = (\mu_1,\mu_2,\mu_3)$ which was chosen by the greedy algorithm. We have obtained $N_{pr,max} = 24$ for the primal problem and $N_{du,max} = 5$. In the Figure 9(b) and 10(b), we represent the error bound $\Delta_N(\boldsymbol{\mu})$ for $1 \le N \le N_{pr/du,max}$. On Figure 11, we represent the solution for $\boldsymbol{\mu} = (1,2,10)$ for different timesteps and control input $g = 1$.

5.4.1. Output

We deal with the output s_N: the average temperature in the duct, for different parameters $\boldsymbol{\mu}$. For the computations, we took $\Delta t = 0.05$ and $n_t = 150$ timesteps, then $t_f = 7.5$. In Figure 12(a), we represent the evolution of the average temperature when the height of the duct increases. The Figure 12(b) shows that the average temperature at $t = t_f$ decreases when the Péclèt grows up. Physically, if the Péclèt is bigger the transport is dominating and then the temperature is lower.

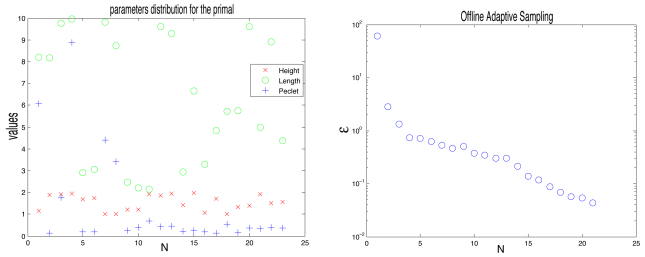

(a) Chosen parameters. (b) Error bound Δ_N.

Figure 9. Sample distribution and greedy error bound for the primal problem.

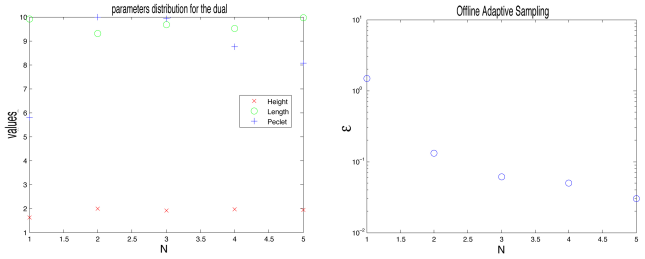

(a) Chosen parameters. (b) Error bound Δ_N.

Figure 10. Sample distribution and greedy error bound for the dual problem.

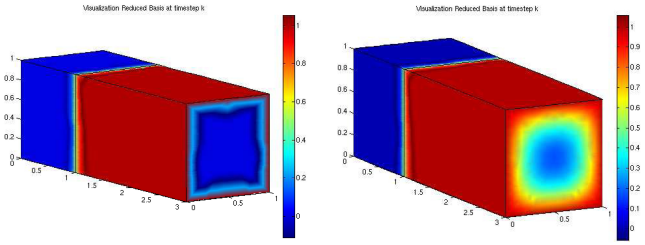

(a) Visualization at $t^0 = 0$. $\Delta_N^s = 0.$. (b) Visualization at $t^6 = 0.3$. $\Delta_N^s = 0.0131$.

Figure 11. Example of representative solution for $\boldsymbol{\mu} = (1, 2, 10)$.

The error bound over the plotted output is $\Delta_N^s(\mu) \leq 10^{-3}$ for all μ tested.

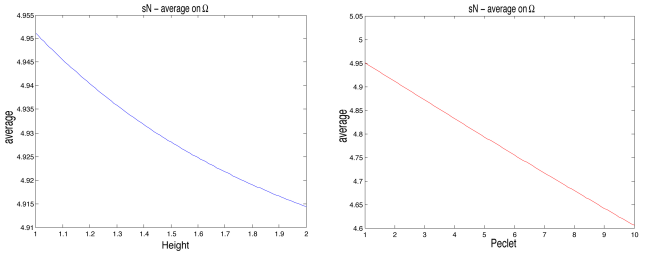

(a) Output with $\mu_2 = 2$ and $\mu_3 = 1$ at $t = t_f$. (b) Output with $\mu_1 = 1$ and $\mu_2 = 2$ at $t = t_f$.

Figure 12.

5.4.2. Computational time

We consider the different computational time measurement we defined previously in Section 4.4.3: ($\mathcal{N} = 2977$)

$$t^{Offline}(\mathcal{N}) = \frac{810.1}{11.3} \approx 72, \qquad t^{Online}(\mathcal{N}, N) = \frac{0.05}{11.3} = 0.005.$$

Then, if we want to compute more than 72 solutions, the use of the RB method is more efficient and recommended. Here, looking also at t^{Online}, we see that the use of the RB method is very gainful. We can get faster Online output evaluation (5 permil of computational costs in the Online evaluation compared with a standard FEM evaluation).

6. Conclusions

This paper extends the application of the RB methods to 3D parametrized heat and mass transfer problems and a comparison/combination with another ROM technique: POD. Results show that the potentialities of the RB methodology and the computational savings are even more significant in the 3D case and with time dependent problems, where a POD-GREEDY combined technique has been applied.

Acknowledgements

We are grateful to Prof. A. Quarteroni (EPFL) and Prof. A.T. Patera (MIT) for support, very useful remarks and suggestions and to the referees who helped in improving this manuscript with their remarks.

References

[1] *Reduced Basis at MIT. http://augustine.mit.edu/methodology.htm*, ©MIT, 2009.
[2] *Comsol Multiphysics* 3.5*a*. Guide available at *http://math.nju.edu.cn/help/mathhpc/document.htm.*
[3] V.S. ARPACI. *Conduction Heat Transfer*. Addison-Wesley, Reading, UK, 1966.
[4] V.S. ARPACI, P.S. LARSEN. *Convection Heat Transfer*. Prentice Hall, Englewood Cliffs, US, 1984.
[5] F. INCROPERA, D. DeWITT, T. BERGMANN, A. LAVINE. *Fundamentals of Heat and Mass Transfer*. John Wiley & Sons, 2007.
[6] B.O. ALMORTH, P. STERN, F.A. BROGAN. *Automatic choice of global shape functions in structural analysis*. AIAA Journal, 16: 525-528, 1978.
[7] D.B.P. HUYNH, N.C. NGUYEN, G. ROZZA, A.T. PATERA. *Documentation for rbMIT Software: I. Reduced Basis (RB) for Dummies, II. Time dependent problems*. ©MIT, available at *http://augustine.mit.edu*, 2008.
[8] G. ROZZA, D.B.P. HUYNH, N.C. NGUYEN, A.T. PATERA. *Real-Time Reliable Simulation of Heat Transfer Phenomena*. ASME Summer Heat Transfer Conference, Proceedings, San Francisco, California USA, Paper HT2009-88212, 2009.
[9] D.B.P. HUYNH, G.ROZZA, S. SEN, A.T. PATERA. *A successive constraint linear optimization method for lower bounds of parametric coercivity and inf-sup stability constants*. Comptes Rendus Mathématique, Volume 345: 3362-3366, 2007.
[10] A.K. NOOR, J.M. PETERS *Reduced Basis technique for nonlinear system analysis of structures*. AIAA Journal, 18(4): 455-462, 1980.
[11] A.T. PATERA and G. ROZZA. *Reduced Basis Approximation and A Posteriori Error Estimation for Parametrized Partial Differential Equations*. To appear in MIT Pappalardo Graduate Monographs in Mechanical Engineering, ©MIT, 2006-2009, Version 1.0.
[12] A. QUARTERONI. *Numerical Models for Differential Problems*. MS& A, Volume 2, Springer, 2009.
[13] A. QUARTERONI, G. ROZZA. *Numerical solution of parametrized Navier-Stokes equations by reduced basis methods*. Numerical Methods for PDEs, 23(4): 923-948, 2007.
[14] G. ROZZA, D.B.P HUYNH and A.T. PATERA. *Reduced Basis Approximation and a Posteriori Error Estimation for Affinely Parametrized Elliptic Coercive Partial Differential Equations : Application to Transport and Continuum Mechanics*. Archives of Computational Methods in Engineering, 15(3):229-275, 2008.

[15] G. ROZZA, N.C. NGUYEN, A.T. PATERA, S. DEPARIS. *Reduced basis method and a posteriori error estimators for heat transfer problems*. ASME Summer Heat Transfer Conference, Proceedings, San Francisco, California USA, Paper HT2009-88211, 2009.

[16] N.C. NGUYEN, G. ROZZA, A.T. PATERA. *Reduced Basis Approximation and A Posteriori Error Estimation for the Time-Dependent Viscous Burgers' Equation*. Calcolo, 46(3):157-185, 2009.

[17] N.C.NGUYEN, G. ROZZA, D.B.P.HUYNH, A.T.PATERA. *Reduced basis approximation and a posteriori error estimation for parametrized parabolic PDEs; Application to real-time Bayesian parameter estimation*. In L. Tenorio, B. van Bloemen Waanders, B. Mallick, K. Willcox, L. Biegler, G. Biros, O. Ghattas, M. Heinkenschloss, and D. Keyes, editors, Computational Methods for Large Scale Inverse Problems and Uncertainty Quantification. John Wiley & Sons, UK, 2010.

[18] J. POMPLUN, F. SCHMIDT. *Accelerated a posteriori error estimation for reduced basis method with application to 3D electromagnetic scattering problems*. SIAM J. Sci. Comp. 32, pp 498-520, 2010.

[19] P. HOLMES, J. L. LUMLEY, G. BERKOOZ. *Turbulence, Coherent Structures, Dynamical Systems and Symmetry*. Cambridge University Press, UK, 1996.

[20] M. GREPL, A.T. PATERA. *A posteriori error bounds for reduced basis approximations of parametrized parabolic partial differential equations*. Math. Modelling Num. Analysis 3^a (1), pp 157-181, 2005.

[21] B. HAASDONK, M. OHLBERGER. *Reduced basis method for finite volume approximations of parametrized linear evolution equations*. Math. Modelling and Numerical Analysis, 42(2), pp 277-302, 2008.